Monthly Notices
of the
ROYAL ASTRONOMICAL SOCIETY

Mon. Not. R. Astron. Soc. **426,** 2089–2106 (2012) doi:10.1111/j.1365-2966.2012.21860.x

Radial migration in disc galaxies – I. Transient spiral structure and dynamics

Rok Roškar,[1,2]★ Victor P. Debattista,[3]† Thomas R. Quinn[2] and James Wadsley[4]

[1]*Institute for Theoretical Physics, University of Zürich, Winterthurerstrasse 190, CH-8057 Zürich, Switzerland*
[2]*Astronomy Department, University of Washington, Box 351580, Seattle, WA 98195, USA*
[3]*Jeremiah Horrocks Institute, University of Central Lancashire, Preston PR1 2HE*
[4]*Department of Physics and Astronomy, McMaster University, Hamilton, ON L8S 4M1, Canada*

Accepted 2012 August 3. Received 2012 August 2; in original form 2011 October 6

ABSTRACT

We seek to understand the origin of radial migration in spiral galaxies by analysing in detail the structure and evolution of an idealized, isolated galactic disc. To understand the redistribution of stars, we characterize the time evolution of properties of spirals that spontaneously form in the disc. Our models unambiguously show that in such discs, single spirals are unlikely, but that a number of transient patterns may coexist in the disc. However, we also show that while spirals are transient in amplitude, at any given time the disc favours patterns of certain pattern speeds. Using several runs with different numerical parameters we show that the properties of spirals that occur spontaneously in the disc do not sensitively depend on resolution. The existence of multiple transient patterns has large implications for the orbits of stars in the disc, and we therefore examine the resonant scattering mechanisms that profoundly alter angular momenta of individual stars. We confirm that the corotation scattering mechanism described by Sellwood & Binney is responsible for the largest angular momentum changes in our simulations.

Key words: galaxies: evolution – galaxies: formation – galaxies: kinematics and dynamics – galaxies: spiral – galaxies: structure.

1 INTRODUCTION

As stellar galactic discs form and evolve, the processes governing their development leave behind a multitude of traces. Massive stars pollute the interstellar medium (ISM) through supernova explosions and stellar winds, endowing subsequent generations of stars with distinct chemical signatures. Similarly, dynamical perturbations, whether they are secular (spiral arms or bars) or due to the hierarchical build-up of mass, sculpt the kinematic properties of stellar populations. Together, these signatures provide a 'fossil record' of a disc's evolution through cosmic time.

Galaxy formation models attempt to match their predictions to this fossil record and attempt to reconstruct the disc's history. For the past thirty years, an implicit assumption has been made in such modelling: stars remain in the same part of the disc forever (e.g. Tinsley 1975; Matteucci & Francois 1989; Boissier & Prantzos 1999; Chiappini, Matteucci & Romano 2001). This simple assumption carries enormous power as it allows one to reconstruct the time evolution of a given quantity (such as metallicity and star formation rate) at a particular radius from present-day, single epoch observations. Such 'static' modelling has been successful in illuminating several critical aspects of disc formation such as the need for infall of low-metallicity gas to solve the G-dwarf problem (Tinsley 1975). Over the past several years, however, this assumption of stars remaining near their birth radii has been firmly shaken by the realization that rapid stellar migrations of several kpc are possible (Sellwood & Binney 2002, hereafter SB02).

The idea that stars may not remain near their birth radii is not new. Wielen (1977) suggested that stellar orbits diffuse in velocity space consequently inducing a drift in the galactocentric radius for an ensemble of stars. This was followed up by Wielen & Fuchs (1985) and applied to the determination of the Sun's birthplace (Wielen, Fuchs & Dettbarn 1996). In Wielen (1977) the diffusion is a relatively slow process driven by random scattering by giant molecular clouds – for observationally constrained velocity dispersions, variations in galactocentric radius of at most few kpc are expected. Instead, in the mechanism described by SB02, migrations of *several* kpc may take place in a few hundred Myr due to very efficient exchange of angular momentum at the corotation resonance (CR).

This exchange of energy and angular momentum at the CR occurs without changing the orbital radial actions therefore retaining the orbital circularity. In addition, the mechanism operates most efficiently for stars on the most circular orbits. These two properties lead to the peculiar result that migrations of several kpc in a Milky

★E-mail: roskar@physik.uzh.ch
†RCUK Fellow.

Way (MW)-size disc are possible without substantial accompanying increase in random motion. The increase in velocity dispersion with age of stars (see e.g. Holmberg, Nordström & Andersen 2009 for the solar neighbourhood) constrains heating processes and thereby also the magnitude of spiral perturbations, so the ability of the CR to redistribute stars substantially without heating excessively is a critical aspect of the CR mixing process. Because the SB02 mechanism involves the CR, the spiral amplitudes must be transient if *redistribution* rather than *trapping* is to occur. In the absence of other perturbations, a steady spiral traps stars on horseshoe orbits – however, if a spiral's amplitude grows and decays on a time-scale comparable to one-half the libration period of a horseshoe orbit, the spiral will merely deposit the star on the other side of the resonance and vanish before pulling it back (SB02).

Unlike steady spirals that can heat the disc only at the Lindblad resonances (Lynden-Bell & Kalnajs 1972), transient spirals can also heat the disc away from the principal resonances (Barbanis & Woltjer 1967; Binney & Lacey 1988; Jenkins & Binney 1990). Consequently, a single spiral can heat the disc enough to prevent any further asymmetric structure formation in just a few rotations (Sellwood & Carlberg 1984). Star formation provides a natural cooling mechanism, continually peppering the disc with young stars born with the galactic velocities of their parent gas clouds. Sellwood & Carlberg (1984) found that in the presence of such cooling, transient spirals keep the disc in a quasi-stable state at a Toomre $Q \sim 2$, which allows for their continual regeneration.

The realization that stars in galactic discs may migrate radially across significant distances has in recent years completely changed the discourse on spiral galaxy evolution. Following SB02, several other theoretical works have further illuminated the complexities that radial mixing introduces for stellar population studies. Lepine, Acharova & Mishurov (2003) investigated the effect of corotation scattering on the disc metallicity gradient. Roškar et al. (2008a, hereafter R08a) showed that radial migration could drastically alter the stellar population properties of outer discs and provided an explanation for the observed gradients across the surface brightness profile break in NGC 4244 (de Jong et al. 2007). R08a predicted that discs with broken exponential profiles should show an inflection in the mean age profile corresponding to the break radius. This has subsequently been confirmed indirectly by surface photometry (Azzollini, Trujillo & Beckman 2008; Bakos, Trujillo & Pohlen 2008) and directly by integral-field spectroscopy (Yoachim, Roškar & Debattista 2010; Yoachim et al. 2012) and resolved-star counts (Radburn-Smith 2012), providing further evidence that radial mixing occurs in external galaxies.

Using the same simulations, Roškar et al. (2008b, hereafter R08b) extended the analysis of R08a and investigated the repercussions of stellar migration for a range of stellar population studies: the solar neighbourhood age–metallicity relation (AMR) and metallicity distribution function (MDF); the evolution of metallicity gradients and the reconstruction of star formation histories from present-day observations of stellar populations in external galaxies. They found that >50 per cent of stars on mostly circular orbits in the solar neighbourhood of their model have come from elsewhere and that migration flattens the AMR and broadens the MDF. They also found that the reconstruction of a star formation history becomes problematic in the presence of migration especially at large radii where the mass in migrated stars approaches or exceeds the cumulative amount of stars formed in situ. R08a,b therefore established the notion that regardless of the method used to observe a galactic disc (unresolved photometry, photometry of resolved stars, spectroscopy of individual stars in the MW) radially migrated stars substantially alter the combined properties of the observed sample, thereby possibly strongly biasing the outcome of any subsequent modelling.

Schönrich & Binney (2009a,b) included a probabilistic prescription of radial migration in a chemical evolution model constrained by MW observables and found that, similarly to R08b, the MDF is broadened and the AMR flattened as a result of migration. They found also that most observational properties and peculiarities of the thick disc can be explained by radial migration. Loebman et al. (2011) explored the formation of the thick disc via radial migration in the *N*-body models of R08a,b and similarly found that simulated trends tend to agree qualitatively with observed thick disc properties from the Sloan Digital Sky Survey (SDSS; Ivezić et al. 2008; Lee et al. 2011). Minchev & Famaey (2010) and Minchev et al. (2011, 2012) argued that apart from corotation scattering as presented by SB02, combined effects of multiple nearby resonances from several different patterns may also be important in driving the redistribution of stars. Their results implied that substantial mixing is possible even if the spiral structure is not transient. Brunetti, Chiappini & Pfenniger (2011) measured the diffusion coefficients in idealized bar-unstable discs and found the CR of the bar to be driving the diffusion, though their models were collisionless and as such did not allow for recurrent spiral activity.

Understanding radial migration is particularly relevant at the present time because of the upcoming surveys designed to study the detailed structure of the MW disc. Studies using data from the SDSS (e.g. Ivezić et al. 2008; Jurić et al. 2008) and its follow-up surveys such as Sloan Extension for Galactic Understanding and Exploration (SEGUE; Yanny et al. 2009; de Jong et al. 2010; Lee et al. 2011) as well as results using data from Radial Velocity Experiment (RAVE; Ruchti et al. 2011; Wilson et al. 2011) have already pushed the current models to their limits in trying to explain the various observed trends and interdependencies in the thick and thin discs. In the coming years, spectroscopic surveys, such as High Efficiency and Resolution Multi-Element Spectrograph (HERMES; Freeman & Bland-Hawthorn 2008) and Apache Point Observatory Galactic Evolution Experiment (APOGEE; Prieto et al. 2008), will obtain high-resolution spectroscopy of millions of stars, allowing finally for 'chemical tagging' of stars into their birth clusters (Freeman & Bland-Hawthorn 2002). Such observations will in principle allow for a direct measurement of stellar radial migration in the MW (Bland-Hawthorn, Krumholz & Freeman 2010). At the same time, the *Gaia* mission will provide a complete 6D map of a 10-kpc sphere centred on the Sun (Perryman et al. 2001), and follow-up spectroscopic surveys will yield vast amounts of complementary chemical abundance data. Finally, the Large Synoptic Survey Telescope (LSST; LSST Science Collaborations 2009) will similarly provide ground-based photometry of the entire sky. To distil these vast data sets and apply them to galactic archaeology, a clear understanding of the radial mixing processes is essential.

In this paper, we explore in detail the properties of self-propagating spiral structure and the causes of the resulting radial migration in simulations from R08a,b and Loebman et al. (2011). We first quantify the spiral structure that forms spontaneously in our simulations and use this analysis as a basis for understanding the causes of radial migration. We also perform a set of numerical tests to explore the robustness of our results to choices of numerical parameters and stochasticity. The paper is organized as follows: in Section 2 we discuss the details of our models; in Section 3 we quantify the spiral structure in our fiducial simulation; in Section 4 we explore the causes of radial mixing; in Section 5 we present several tests of the effects of numerical parameters on the

generation of spiral structure and finally, we state our conclusions in Section 6.

2 SIMULATIONS

The initial conditions for all of the runs presented here are generated as described in Kaufmann et al. (2006, 2007), and consist of spherical distributions of dark matter (DM) and gas following a Navarro–Frenk–White (NFW; Navarro, Frenk & White 1997) density profile. The random velocities of the DM particles are initialized to ensure equilibrium by means of the distribution function obtained from an inversion of the NFW density profile (Kazantzidis, Magorrian & Moore 2004). The gas is initialized to the same mass distribution with a temperature profile to yield an approximate hydrostatic equilibrium. The gas is also given a spin consistent with values obtained from collisionless cosmological simulations (Bullock et al. 2001; Macciò et al. 2007), i.e. $\lambda = (J/G)\sqrt{|E|/M^5} = 0.039$, where J is the total angular momentum, E is the total energy of the system and M is the mass. The angular momentum follows a radial profile of $j \propto r$, where j is the specific angular momentum. In the fiducial run we use 10^6 particles per component, resulting in DM particle mass of $10^6\,\mathrm{M}_\odot$ and initial gas mass of $1.4 \times 10^5\,\mathrm{M}_\odot$.

The simulations were run using the code GASOLINE (Wadsley, Stadel & Quinn 2004), a hydrodynamics extension of the parallel multistepping N-body code PKDGRAV (Stadel 2001). The tuning of the subgrid star formation and feedback prescriptions are described extensively in Stinson et al. (2006). Here we summarize the important features. A gas particle becomes eligible for star formation when its density exceeds $0.1\,\mathrm{cm}^{-1}$ and its temperature dips below 15 000 K. If eligible, the gas particle converts some of its mass into a star particle at a rate given by

$$\frac{\mathrm{d}\rho_\star}{\mathrm{d}t} = c_\star \frac{\rho_{\mathrm{gas}}}{t_{\mathrm{dyn}}}, \quad (1)$$

where $c_\star$ is the star formation efficiency (set to 0.05 in all of the simulations), ρ_{gas} is the gas density and t_{dyn} is the local dynamical time. Star particles form with one-third of the initial gas particle mass (in the fiducial simulation this translates to star particle masses of $4.7 \times 10^4\,\mathrm{M}_\odot$) and to avoid unreasonably small particle masses, gas particle masses are limited to one-fifth of their initial mass. When a particle crosses this threshold its mass is distributed among neighbouring particles, resulting in an overall decrease of the number of gas particles with time. Each star particle represents an entire stellar population and therefore a spectrum of stellar masses described by the Miller–Scalo initial mass function (Miller & Scalo 1979). The evolution of massive stars is followed and a feedback cycle is initiated to reflect the explosion of Type II supernovae. At typical particle masses of $\sim 10^4\,\mathrm{M}_\odot$, the supernova energy is injected into the ISM 'in bulk', i.e. individual explosions are not modelled. The effect of the supernova explosions is modelled on the subgrid level as a blast wave propagating through the ISM. We track ISM metal enrichment from Type II and Type Ia supernovae as well as from asymptotic giant branch (AGB) stars.

The complete set of parameters used for the simulations discussed in this paper is listed in Table 1. Our fiducial run has been studied extensively and we used it previously for results presented in R08a,b. The baryonic particles in the fiducial run use a softening length $h_{\mathrm{s}} = 50$ pc. We tested the softening dependence of our results with runs S1, S3 and S4 ($h_{\mathrm{s}} = 25$, 100 and 500 pc, respectively). We also tested the effect of varying particle numbers in runs R1, R3 and R4 with 0.5×10^6, 2×10^6 and 4×10^6 particles in each component, respectively. We ran a further test of the effects of the mass resolution of the DM halo by running a simulation with 10 times the number of DM particles (run SDM). All runs were carried out for 10 Gyr.

Table 1. Simulation parameters.[a]

Name	N_{gas}	N_{dark}	h_{s} (kpc)
Fiducial[b]	10^6	10^6	0.05
S1	10^6	10^6	0.025
S3	10^6	10^6	0.1
S4	10^6	10^6	0.5
SDM	10^6	10^7	0.05
T2[c]	10^6	10^6	0.05
T3[c]	10^6	10^6	0.05
R1	5×10^5	5×10^5	0.05
R3	2×10^6	2×10^6	0.05
R4	4×10^6	4×10^6	0.05
R1-T2[d]	5×10^5	5×10^5	0.05

[a]All runs have $M_{\mathrm{vir}} = 10^{12}\,\mathrm{M}_\odot$, $\lambda = 0.039$ and $c = 8.0$.
[b]This is our fiducial run that was presented previously in R08a,b.
[c]Runs T2 and T3 are identical to the fiducial run S2/R2 but use different random seeds when generating the initial conditions.
[d]Run R1-T2 is identical to run R1 but initialized with a different random seed.

The opening angle Θ used for simplifying gravity calculations was 0.7 for all runs. The code uses a multistepping scheme with the condition that a particle's time-step $\Delta t_{\mathrm{grav}} = \eta(\epsilon/a)^{1/2}$, where $\eta = 0.175$, ϵ is the gravitational softening length and a is the acceleration. For the gas particles, the time-step must also satisfy $\Delta t_{\mathrm{gas}} = \eta_{\mathrm{courant}} h/[(1+\alpha)c + \beta\mu_{\mathrm{max}}]$, where $\eta_{\mathrm{courant}} = 0.4$, h is the smoothed particle hydrodynamics (SPH) smoothing length, $\alpha = 1$ is the shear coefficient and $\beta = 2$ is the viscosity coefficient. μ_{max} is described in Wadsley et al. (2004). The SPH quantities were calculated on a kernel using 32 nearest neighbours. The cooling in all runs is calculated without taking into account the metal content of the gas. Additional simulations where we vary the physical parameters of the initial haloes (mass, angular momentum) will be presented in Paper II of this series.

The strength of these idealized models lies in the fact that there is no initial stellar component, so none of the properties of the disc is chosen a priori. As soon as the simulation begins, the gas is allowed to cool in the potential well of the DM, and as it reaches densities and temperatures conducive to star formation (as set by our star formation parameters) it spawns stars. Because of the spin, the gas naturally settles into a rotationally supported disc in the centre of the halo, giving rise to a galactic disc composed of a mix of stars and gas. Thus, although all of the simulations presented here are idealized in the sense that the discs evolve in isolation the simulations also depart sharply from most other work using idealized discs because we do not *construct* equilibrium disc models, as is usually done in studies focusing on dynamical effects (e.g. Debattista et al. 2006). Instead, our models grow discs spontaneously without any biases regarding disc structure or stellar population properties. The spontaneous growth is particularly important for the development of self-limiting structure and subsequent secular evolution (e.g. Sellwood & Carlberg 1984). We are therefore able to follow the temporal evolution of stellar populations and make direct comparisons between simulated properties and observed galaxies with unprecedented detail.

Real discs of course do not form in such a simple way, but our simulations are meant only to mimic the formation of discs after

the last major merger. For massive galaxies ($M \geq 10^{11}\,\mathrm{M}_\odot$) disc formation is not dominated by filamentary accretion after $z \sim 2$ (Kereš et al. 2005; Brooks et al. 2009). Minor mergers may influence the morphology of the disc (e.g. Kazantzidis et al. 2008), but the majority of the disc fuel comes from quiescent cooling of gas from the halo.

By limiting the processes included in our models, we can perform a cleaner analysis[1] of the disc dynamics. Because of lower computational cost compared to fully cosmological simulations, we are also able to attain higher resolution. At the fiducial resolution, for example, the discs have ∼2.5 million star particles by 10 Gyr – typical hydrodynamic cosmological simulations of $10^{12}\,\mathrm{M}_\odot$ galaxies have a few times fewer disc particles.[2] However, by allowing our discs to form spontaneously without a pre-defined stellar component, we can follow the evolution of stellar populations self-consistently throughout the simulation.

3 ANATOMY OF SPIRALS

We begin by dissecting the spiral structure in our fiducial simulation to show that spirals are responsible for the migration of stars. For several decades, idealized N-body simulations have produced self-limiting, transient spirals arising from various sources of instability, such as Poisson noise, discontinuities in the distribution function (Sellwood & Kahn 1991) or stimulation by the central bar (Debattista et al. 2006). Studies of the evolution of transient spiral structure have largely been confined to the realm of carefully tuned N-body experiments, sometimes with an addition of gas hydrodynamics or an ad hoc cooling mechanism (Sellwood & Carlberg 1984). Cooling is essential for the persistence of transient spirals because spirals are naturally self-destructive: when they form, they also very efficiently heat the disc. Controlled and carefully tuned N-body experiments are vital for understanding the orbit response of the underlying disc to perturbing wave propagation, but do not adequately address how spontaneously recurring patterns may affect stars in a real disc. SB02 (their figs 10–12) provide a hint and show that an unconstrained collisionless simulation produces an array of spirals, identified by local maxima in the power spectrum of $m = 2$ perturbations. In this section, we seek to expand on such analysis by also considering the temporal evolution of patterns.

In our simulations, the stellar discs are cooled naturally by ongoing star formation. Stars are initially on kinematically cool orbits inherited from their parent gas particles, continuously infusing the disc with a population susceptible to supporting instabilities. The spiral structure manifests, as we show below, in a complicated array of patterns and pattern speeds that evolve as the disc grows. Fig. 1 shows the Toomre $Q \equiv \sigma_R \kappa / 3.36 \Sigma G$ parameter as a function of radius at several different times, where σ_R is the radial velocity dispersion of the stars, κ is the epicyclic frequency, Σ is the surface density of stars and G is the gravitational constant. The bottom panel shows Σ and σ_R separately. The recurring spirals are possible because the disc establishes a marginally stable state, with $Q \sim 2$ in the main part of the disc at all times.

[1] We analyse the simulations using our own IDL routines as well as the publicly available PYTHON-based PYNBODY package: http://code.google.com/p/pynbody/

[2] Cosmological simulations may have larger numbers of particles in the system, but most comprise the other galactic components like the bulge and halo and relatively few are found in the disc component.

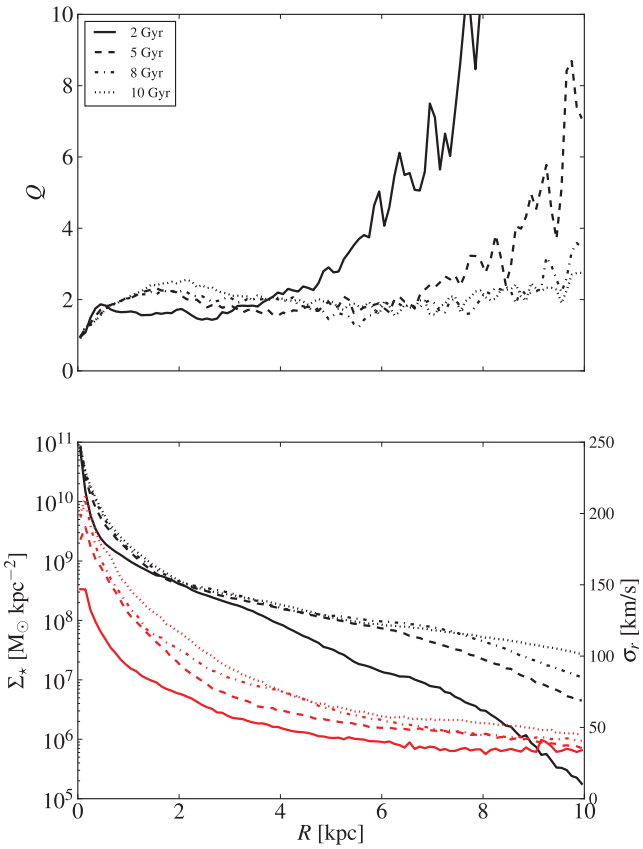

Figure 1. Top: Toomre Q parameter as a function of radius at four different times in the fiducial run. Bottom: stellar surface density (black) and radial velocity dispersion (red). Line types correspond to the same times as in the upper panel.

In order to study the spiral structure, we centre the system on the potential minimum and divide the particles into concentric equal-width radial bins. We then expand the stellar particle distribution in a Fourier series given by

$$\Sigma(r, \phi) = \sum_{m=0}^{\infty} c_m(r)\, \mathrm{e}^{[-\mathrm{i}m\phi_m(r)]}, \tag{2}$$

where r is the radius, m is the pattern multiplicity, and $\phi_m(r)$ is the phase of the mth mode at radius r. The complex coefficients $c_m(r)$ are given by

$$c_m(r) = \frac{1}{M(r)} \sum_{j=1}^{N} m_j\, \mathrm{e}^{\mathrm{i}m\phi_j}, \tag{3}$$

where $M(r)$ is the total mass in the radial bin, m_j is the particle mass, ϕ_j is the angle between the particle's position vector and the x-axis and N is the total number of particles in the bin satisfying $r < r_j < r + \delta r$. Strictly speaking, this type of decomposition will identify any type of azimuthal m-fold symmetry, but our assumption is that strong components identified in this way with low m will be due either to a bar or spirals. The bar can be separated from spirals by virtue of its constant phase as a function of radius; however, beyond the central few kpc we can reasonably expect this method to identify spirals.

Fig. 2 shows stellar density maps with contours of $m = 1$ through $m = 4$ Fourier components, obtained using equations (2) and (3), demonstrating that our method can reliably identify and account for the underlying disc structure. It is also apparent from Fig. 2 that there

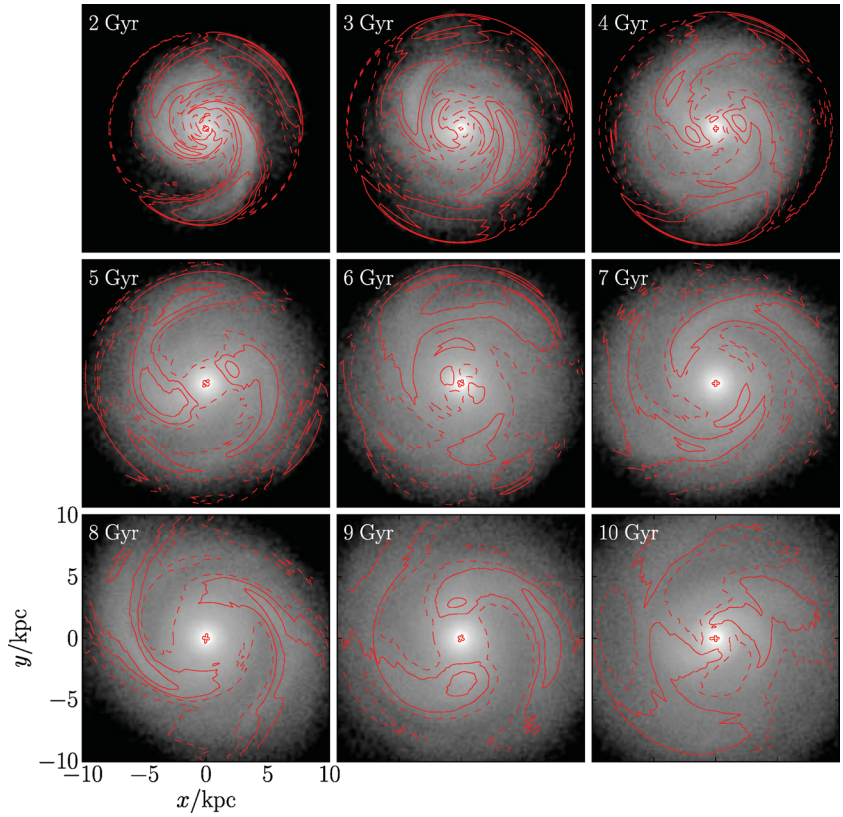

Figure 2. Stellar density maps for the fiducial run at several times. Contours of overdensities reconstructed from the Fourier coefficients for $m = 1$ to $m = 4$ are overlaid in red. Contours are drawn at the −50, −20, −5, 5, 20 and 50 per cent (under)overdensities; negative contours are shown with dashed lines. We also require that each radial bin has at least 1000 particles to avoid noise that may arise in regions with low particle numbers. All panels are the same physical scale.

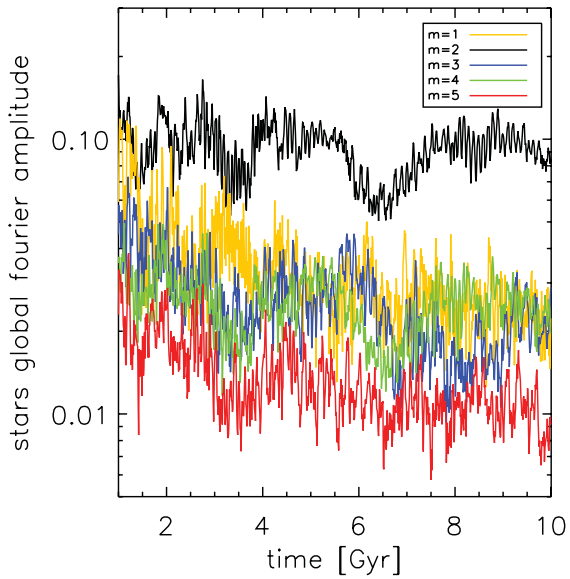

Figure 3. Global Fourier amplitudes of the stellar particles for $m = 1$ through $m = 5$ Fourier components.

are often distinct spirals present at different radii and that each spiral often has a narrowly defined peak overdensity. The overdensities we measure vary with time but the normalized amplitude of the $m = 2$ mode $A_2 \equiv |c_2| \leq 0.4$ at all times for all runs, compatible with the observations of Rix & Zaritsky (1995). Overdensities at the level of a few per cent are difficult to see by eye in the stellar surface density map, but are easily identified with a Fourier decomposition.

In a spontaneously evolving disc, we expect patterns of all multiplicities to exist, and they all could perturb the orbits of stars. In Fig. 3 we show the global Fourier amplitude as a function of time for $m = 1$ through $m = 5$ Fourier components. The $m = 2$ mode dominates at all times in this simulation. We therefore focus our dynamical analysis on the $m = 2$ mode, though we cannot exclude that the other components also contribute some small fraction to the angular momentum redistribution in the disc.

The greatest impact of spiral structure on the orbits of stars occurs at resonances, which are narrow regions in phase space satisfying $m(\Omega_\phi - \Omega_\mathrm{p}) = l\kappa$, where m is the pattern multiplicity, Ω_ϕ and κ are the azimuthal and radial frequencies of the orbit and Ω_p is the spiral's pattern speed. If $m = 2$, setting l to ± 1 gives the inner and outer Lindblad resonances (ILR and OLR), and $l = 0$ corresponds to the CR. To identify resonances, we must therefore obtain Ω_p, which can be achieved using our Fourier decomposition.

We can estimate the instantaneous Ω_p at radius r simply by performing numerical differentiation $\Omega_\mathrm{p} = \frac{\partial}{\partial t}\phi_m(r)$ or, equivalently, obtaining a linear fit to $\phi_m(r)$ as a function of time. This method is reliable if there is a single steady perturbation at the radius in question, and studies of bars usually employ this method to recover the bar pattern speed (e.g. Debattista & Sellwood 2000; Dubinski, Berentzen & Shlosman 2009). We find, however, that for our purposes this is insufficient because spirals of varying strengths and

pattern speeds are present at all radii, and this method only ever identifies the most prominent pattern.

To reliably identify multiple pattern speeds in the disc, we require a different method. Ideally, the method would not only allow us to identify patterns at a given time interval, but it would also give us information about the evolution of these patterns with time. However, because the coefficients $c_m(r)$ are calculated at each output, they comprise a time series and we can obtain a further discrete Fourier transform of this series, given by

$$C_{k,m}(r) = \sum_{j=0}^{S-1} c_j(r,m) w_j \, \mathrm{e}^{2\pi \mathrm{i} jk/S}, \qquad k = 0, \ldots, S-1$$

(Press et al. 1992), which yields the Fourier coefficients at discrete frequencies Ω_k, and $c_j(r, m)$ is the coefficient at time $t = t_0 + j\Delta t$, radius r and multiplicity m. S is the number of samples, in this case the number of outputs at which we evaluate the structure. We use a Gaussian window function,

$$w_j(x) = \mathrm{e}^{-(x-S/2)^2/(S/4)^2},$$

to avoid high-frequency spectral leakage (using other window functions such as the Hanning window has no appreciable effect). The frequency sampling is determined by the length of the baseline and Δt, the time between samples (outputs),

$$\Omega_k = 2\pi \frac{k}{S\Delta t} m, \qquad k = 0, 1, \ldots, \frac{S}{2},$$

where $\Omega_{\rm Ny} \equiv \Omega_{k=S/2}$ is the Nyquist frequency. We are here faced with a choice between spectral resolution and the ability to identify 'instantaneous' pattern speeds. If the baseline used is too long, the power spectrum will show a large number of patterns not all of which are important for the disc at any particular time. We find that at our time-step resolution of 10 Myr, using a 1-Gyr (100 time-steps) baseline gives satisfactory spectra, though the resolution is still rather coarse at $\sim$3 km s^{-1} kpc^{-1}. This sampling rate gives a Nyquist frequency of $\Omega_{\rm Ny} = 153$ km s^{-1} kpc^{-1} for $m = 2$ structure.

We can now construct a power spectrum at each radius given by

$$P(\Omega_k, r) = \frac{1}{W}\left[|C_k(r)|^2 + |C_{S-k}(r)|^2\right], \quad k = 1, 2, \ldots, \frac{S}{2} - 1,$$

where $W \equiv S\sum_{j=0}^{S} w_j$ is the normalization factor taking into account the windowing function (Press et al. 1992). We assume that the periodic changes will be due to the phase, rather than amplitude variations, thus giving us pattern speeds (Sellwood & Athanassoula 1986). The resulting combined power spectrum across the whole disc gives us information about the strengths of patterns as a function of radius, and is shown in Fig. 4. The contours in the panels on the left show the frequency power spectrum as a function of radius, while the right-hand panel shows the integrated power over the whole disc at each frequency.

The pattern speeds in the given segment of the disc evolution can now be obtained by extracting the peaks from the radially integrated frequency spectrum. We measure the peaks by fitting Gaussians to the local maxima in the integrated spectrum. To reliably identify overlapping features in the spectrum we use an iterative procedure, which progressively removes the most prominent peaks identifying lesser peaks on subsequent passes. In this way, we identify the three most important patterns. We use the Gaussian fit parameters to estimate peak amplitudes and pattern speeds. The horizontal lines in the left-hand panel of Fig. 4 correspond to the pattern speeds obtained in this way and illustrate that this method can recover the major pattern speeds well. The solid and dashed black lines show Ω_c, the circular frequency, and $\Omega_c \pm \kappa/2$ – ILR, CR and OLR

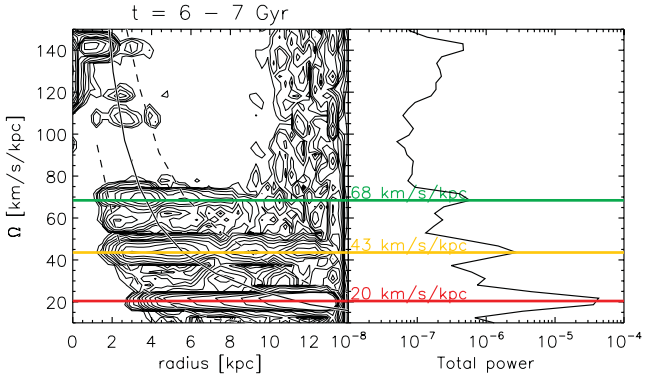

Figure 4. Left: power spectrum of $m = 2$ frequencies as a function of radius in the disc, for the time interval 6–7 Gyr. The solid black line marks Ω_c, while the dashed black lines mark $\Omega_c \pm \kappa/2$. The three main spiral patterns are identified by coloured horizontal lines. Right: the global frequency spectrum. Contour levels vary in logarithm from 5×10^{-10} to 1×10^{-6}.

resonances exist for stars on nearly circular orbits where the pattern speed lines intersect one of these loci, from left to right, respectively.

Fig. 4 reveals the richness of spiral structure in a spontaneously evolving disc. The range of radii that may be influenced by resonances from any of these patterns spans essentially the entire disc. However, Fig. 4 only tells us about the patterns present in a given time interval – we would like to know how these patterns evolve with time.

To extract time information from our data, we repeat the above procedure at equally spaced time intervals. We show such a result in Fig. 5. The dominant frequencies are shown as a function of time, identified using the procedure outlined above, with individual point sizes reflecting the normalized amplitude of each perturbation. Each point on the plot uses a baseline of 1 Gyr of data to generate the power spectrum as discussed above, so that at each time t the patterns shown reflect disc evolution from $t - 1$ Gyr to t. Hence, adjacent points represent overlapping data and the point sizes reflect a time-averaged amplitude. The instantaneous amplitudes vary on

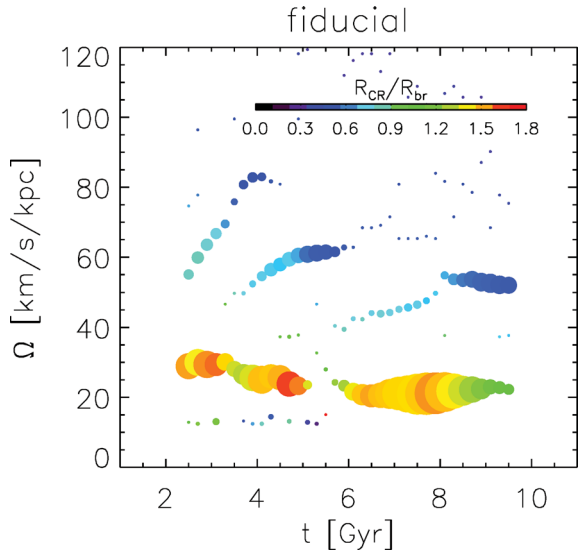

Figure 5. Perturbation frequencies in the disc as a function of time obtained via the WFFT (see text). Point sizes reflect the normalized amplitude of each perturbation. Colour denotes the ratio of corotation radius to the disk surface density break radius.

much shorter time-scales as the spirals flicker in and out of existence. Colours of the points correspond to the ratio of each pattern's corotation radius to the radius of the disk surface density break, which marks the transition to the outer disk.

It is striking that the perturbation at $\Omega_p \sim 20$–$30\,\mathrm{km\,s^{-1}\,kpc^{-1}}$ dominates through most of the disc's lifetime. This perturbation is very steady except for a brief decrease at 5.5 Gyr and a subsequent strong growth peaking at 7.5 Gyr. The brief period of decreased power can also be identified in the panels of Fig. 2, which show that between 5 and 6 Gyr the patterns become significantly disordered. Fig. 5 also shows that perturbations with larger frequencies are significantly more short-lived. We can identify three separate strong perturbations with $\Omega_p > 50\,\mathrm{km\,s^{-1}\,kpc^{-1}}$, the most persistent of which survives for ∼2 Gyr.

The time evolution of pattern speeds and amplitudes shown in Fig. 5 provides a new look at the temporal evolution of the disc. We double checked that the signal extracted using the windowed fast Fourier transform (WFFT) method is indeed real by performing an independent analysis using a continuous wavelet transform (CWT), because it is specifically tailored to recover the time evolution of frequencies in a signal. The CWT yields qualitatively identical results to the WFFT – however, we found it less cumbersome to quantify the results (i.e. determine pattern speeds and amplitudes) using the WFFT.

While Fig. 5 shows the evolution of frequencies, it does not allow one to infer the amplitude variations of individual patterns because the WFFT is performed on 0.5 Gyr intervals. Therefore, while we do see variation in the sizes of the points, corresponding to amplitude changes, there is a possibility that we are hiding shorter time-scale fluctuations.

We attempt to reconstruct the amplitude variation of individual patterns directly by using a band-pass filter in frequency space and then using the inverse Fourier transform to obtain the time series of Fourier coefficients representing the density perturbation. The band pass is centred roughly on the desired frequency and is $10\,\mathrm{km\,s^{-1}\,kpc^{-1}}$ wide. The choice of width is somewhat arbitrary, but we find that the patterns are reasonably well separated with this choice.

Fig. 6 shows the resulting amplitude variations for the three principal patterns found in Fig. 4. The oscillatory amplitude transience of spirals on Gyr time-scales in our run is clearly visible. Note that

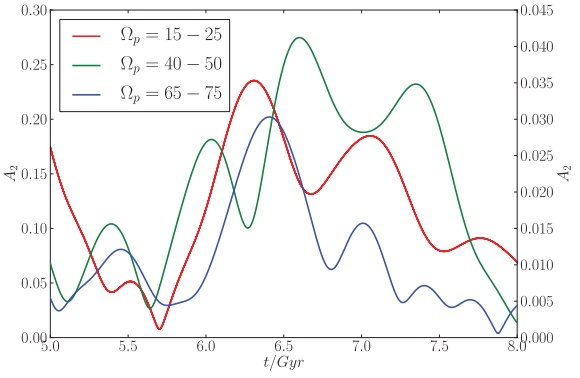

Figure 6. Amplitude variation as a function of time for the three main patterns identified in Fig. 4. The amplitudes are obtained by using a band pass of $10\,\mathrm{km\,s^{-1}\,kpc^{-1}}$ centred on each frequency and at a radius corresponding to the corotation radius at 7 Gyr (i.e. identified using the power spectrum of Fig. 4). Because the amplitudes of the faster patterns are quite different, we use the left y-axis for the 20–30 $\mathrm{km\,s^{-1}\,kpc^{-1}}$ pattern (red line), and the right y-axis for the other two (green and blue lines).

apart from the slowest pattern, the pattern speeds are also evolving on ∼Gyr time-scales (see Fig. 5). However, while the evolving pattern speeds mean that resonances associated with these patterns are sweeping through the disc, our system does not produce a multitude of strong features of a wide range of pattern speeds at any given time. Thus, the transience in the system described here might be somewhat different from that found in other works.

4 ANGULAR MOMENTUM EXCHANGES AT COROTATION IN THE SIMULATIONS

In the previous section, we demonstrated that the disc in our simulation harbours a variety of spiral patterns of various pattern speeds. We now discuss how these patterns influence the orbits of stars. In particular, we try to understand whether the radial migration in our growing, unconstrained disc can be explained by the CR scattering described in SB02 alone, or whether we must invoke more complex mechanisms to explain the observed behaviour.

Fig. 7 illustrates the diversity of individual stellar orbital histories in the disc. These orbits were chosen from a random set of particles that are found beyond 3 kpc at the end of the simulation, in order to illustrate the range of possible orbital histories. It is clear from these examples that stars may migrate rapidly while retaining a nearly circular orbit, and that a circular orbit does not imply a radially static history. In fact the instantaneous appearance of an orbit says very little about the star's history, as it is evidently possible to even circularize a significantly eccentric orbit (see e.g. the upper right-hand panel).

In Fig. 8 we show the changes in angular momentum as a function of initial particle angular momentum.[3] For the bottom panel, the perturbations dominating the disc during this time are the same ones we identified in Fig. 4. Note that the baseline used to obtain the frequency power spectrum is 1 Gyr, but the time-scale on which we consider Δj_z versus j_z is 0.5 Gyr, where $j_z = [\boldsymbol{r} \times \boldsymbol{v}]_z$ and $\Delta j_z = j_z(t_2) - j_z(t_1)$. If we use a 1-Gyr baseline (which corresponds to >4 rotation periods at 5 Gyr and 8 kpc) we find that the signature of spiral scattering in the Δj_z versus j_z plane becomes too smeared to be useful. On the other hand, a 0.5-Gyr baseline is insufficient to reliably identify pattern speeds in the power spectrum, so we are forced to accept this small inconsistency. The higher frequency perturbations may evolve considerably during ∼1 Gyr, but the resonance loci are not a particularly steep function of R (Fig. 4) so we can still obtain approximate locations of resonances. In Fig. 6 we can see that during 6.5–7 Gyr we may expect the disc to be largely dominated by the growth of the $45\,\mathrm{km\,s^{-1}\,kpc^{-1}}$ pattern. However, during the 5.3–5.5 Gyr time interval, we see that the two faster patterns are growing at the same time. It is also apparent from Fig. 5 that around this time the faster pattern dominates the overall perturbation amplitude in the main part of the disc. We therefore choose this second time interval to look for non-linear effects stemming from resonant coupling of multiple perturbations (e.g. Quillen 2003; Minchev & Famaey 2010).

In both cases, the dominant pattern causes the characteristic antisymmetric shape in Δj_z versus j_z associated with CR orbit swapping (SB02). The few dominant patterns we identify cannot explain the full structure seen in either panel, however. In Fig. 4 we can see that some amount of power is present in subtler patterns not picked up by our automated algorithm, such as at ∼30 and ∼60 $\mathrm{km\,s^{-1}\,kpc^{-1}}$.

[3] Throughout the paper we use the notation that specific angular momentum is lowercase j and total angular momentum is capital J.

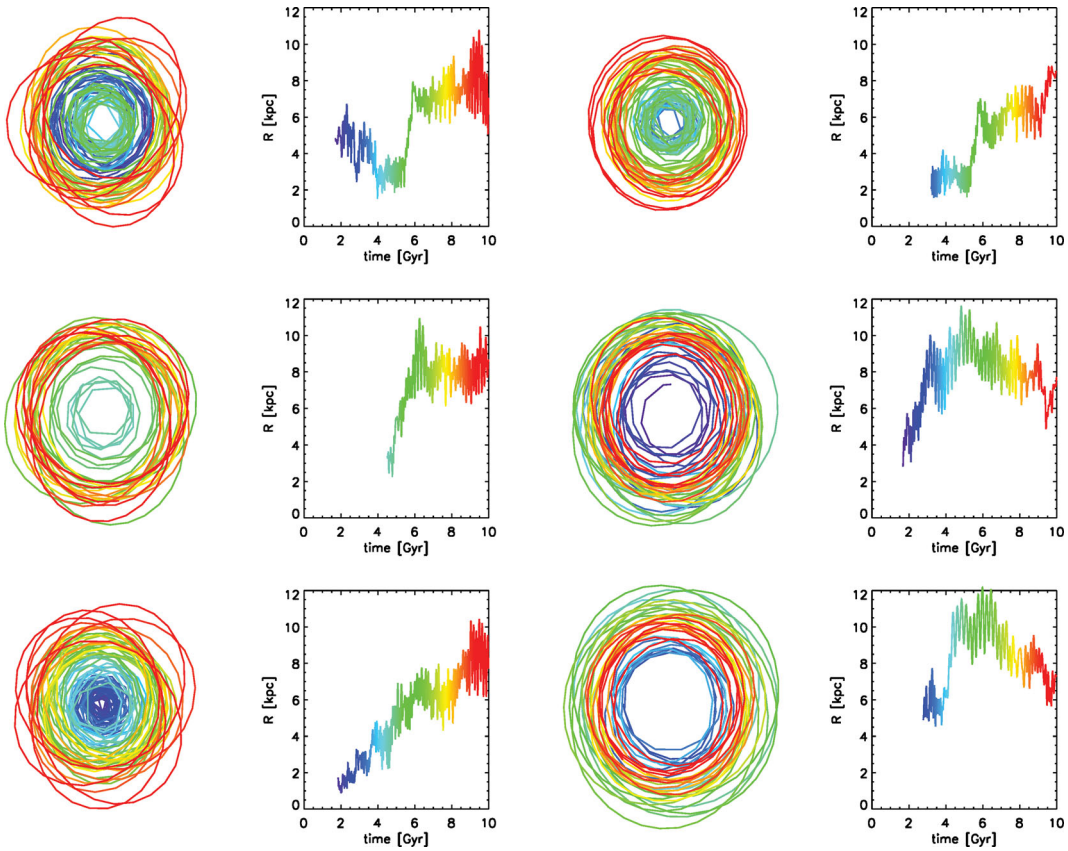

Figure 7. Some examples of orbits from the fiducial simulation. Orbits are coloured according to time to make the temporal evolution more apparent, with blue corresponding to early and red to late times. Stars can migrate inwards and outwards very rapidly without substantially increasing their eccentricities.

Some of the structure in Fig. 8 must therefore also be due to those patterns, which may be in the process of growing or fading at either end of the time interval we consider. Another possibility is that patterns of higher multiplicity contribute to some of the angular momentum exchange. The prominent feature seen in the very inner part of the disc in the top panel is a short-lived weak bar instability. Note the scale of Δj_z: in both panels the changes caused by the dominant pattern approach 50 per cent of j_z. The changes are especially drastic in the top panel, given the short time interval we are considering.

4.1 Corotation crossing and chaos

A *steady* spiral perturbation does not result in angular momentum exchange at the CR because stars are trapped on horseshoe orbits. If the spiral is transient, however, the trapping does not occur and stars can traverse from one side of the CR to another. We look for such horseshoe orbits during the time interval 6.5–7 Gyr among the particles with $|\Delta j_z| > 200$ (roughly the top 10 per cent of migrators) around the CR with the 43 km s^{-1} kpc^{-1} pattern shown in the bottom panel of Fig. 8. We plot the orbits of a random subset of these particles in a frame corotating with the spiral in columns 1 and 3 of Fig. 9. The orbits are coloured according to the relative strength of the 43 km s^{-1} kpc^{-1} spiral at any given time, shown in the bottom right-hand panel. The radius as a function of time is shown as a black line in columns 2 and 4. In the corotating frame, a particle crossing the CR also reverses direction. All particles cross the CR at almost the same time, near the peak of the spiral amplitude, but the orbits are otherwise largely unperturbed. Furthermore, all inward and outward migrations are, respectively, correlated in azimuth. For example, see the outward migrators in panels 1, 2 and 3 and the inward migrators in panels 6 and 7. This hints at the CR being responsible for the migration because one expects the particles trailing the spiral arm to preferentially be pulled outward and vice versa for those particles leading the arm.

In Fig. 10 we demonstrate that this is indeed the case by plotting the density of inward and outward migrators (in red and blue, respectively – darker colours indicate higher density) for the 5.3–5.5 Gyr time interval (top panel) and 6.5–6.7 Gyr time interval (bottom panel). Spiral overdensity, reconstructed from $m = 2$ through $m = 4$ Fourier components, is shown in black contours. The first interval is chosen because it is near the time when two of the patterns are peaking simultaneously, while during the later time interval only the 43 km s^{-1} kpc^{-1} spiral peaks. Note that we did not select these particles specifically to isolate ones interacting with either spiral. The only selection criterion is that in the given time interval they are in the top 5 per cent of migrators. However, essentially all of the migration in both time intervals is occurring around the CRs with most of the inward and outward migrators, respectively, leading and trailing the dominant spiral. Low densities of migrators extend to other regions of the disc where other spirals play a role, but the majority of migration is taking place around the 43 km s^{-1} kpc^{-1} spiral, as expected from Fig. 8. The dashed green circle corresponds to the CR of the 43 km s^{-1} kpc^{-1} spiral and passes directly through the centres of the highest density regions of migrators.

The top panel, showing the migrators for the time interval where two of the faster patterns are peaking simultaneously, shows very similar behaviour to the bottom panel where only one pattern is

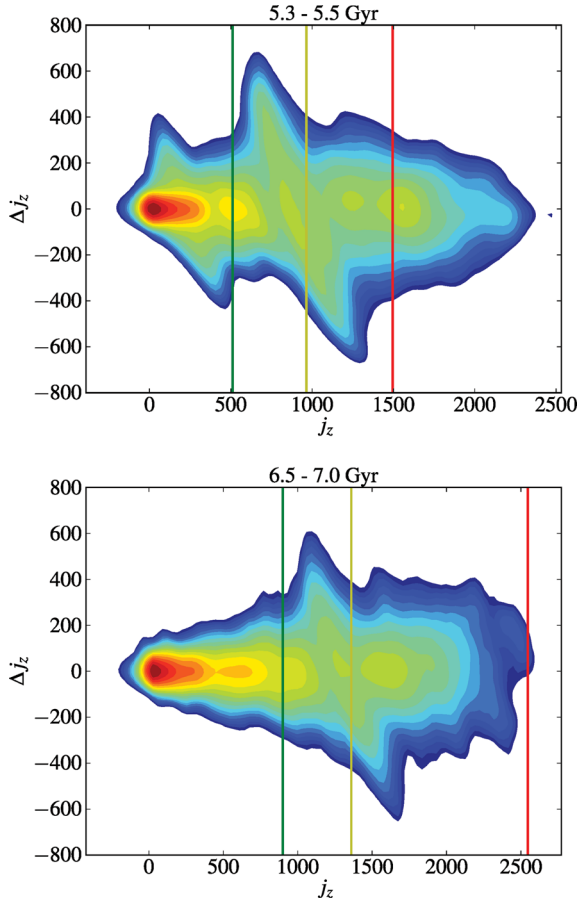

Figure 8. Distributions of Δj_z given initial j_z for all particles in the simulation between 5.3 and 5.5 Gyr (top panel) and 6.5 and 7.0 Gyr (bottom panel). The CRs of the main perturbations found at each time are marked by vertical lines, with the colours in the top panel corresponding to the colours in Fig. 4. The logarithmically spaced contour levels are the same for both panels and correspond to mass density.

dominating. If the overlap of resonances was causing chaotic evolution, it should manifest itself during such a time interval (the dominant patterns are ∼65 and 30 km s^{-1} kpc^{-1}). Around a radius of 5 kpc in the top panel, the density of both inward and outward migrators is saturated, implying that the migration is even more dominated by a single pattern in this time interval. The physical locations of the migrators are strongly clustered around the individual overdensity peaks. In this interval, there is also a weak oval feature in the centre, driving some angular momentum exchange in the inner part the disc (see the top panel of Fig. 8). The dashed green circle in this panel corresponds to the CR of the 65 km s^{-1} kpc^{-1} spiral, which is clearly where most of the angular momentum exchange is occurring. Thus it is evident that even when multiple strong patterns are present near their amplitude peaks, the majority of angular momentum exchange occurs at very predictable locations, i.e. on either side of overdensity peaks and at their CR. The migration in this earlier time interval is stronger, hinting at the possibility that different patterns may help feed each other's CR zones. However, as we show in the following paragraphs, we are unable to find clear indications of non-linear or chaotic evolution.

In columns 2 and 4 of Fig. 9 we show the CWT power scalogram of the x component of the orbits shown in columns 1 and 3. We construct the power scalogram by using the Morlet–Grossmann wavelet whose basis 'mother' wavelet is given by

$$\Psi_0(t) = \frac{1}{\sqrt{(2\pi)}}\, \mathrm{e}^{-t^2/2\sigma^2}\, \mathrm{e}^{-\mathrm{i}\omega_0 t}.$$

See Daubechies (1990) for a thorough theoretical introduction to wavelets and Torrence & Compo (1998) and Nener, Ridsdill-Smith & Zeisse (1999) for a practical guide. We use the approach described in the latter two for calculating our wavelet power scalograms. The y-axis in the spectrograms in Fig. 9 represents wavelet scale, which is proportional to the inverse of frequency. We can therefore follow the time evolution of dominant frequencies by inspecting the most prominent ridges in the scalogram. Note that we plot the logarithm of the power, so many of the smaller features are orders of magnitude weaker than the obvious dominant ridges. Chaotic systems can be identified with this method because the ridges in the scalogram show significantly irregular curvature and discontinuities (Chandre, Wiggins & Uzer 2003; Gemmeke, Portegies Zwart & Kruip 2008).

Chandre et al. (2003) show that in chaotic systems, ridges in the scalogram become shorter, bent and disordered. In our case, we find in general mostly horizontal features extending across much of the entire time interval during which migration takes place. As the stars cross corotation and migrate in radius, the dominant frequency has to change and this is reflected in the bend apparent in the main ridge in all the panels. However, there is no evidence of significantly scattered and bent ridges (see e.g. fig. 4 in Gemmeke et al. 2008 and fig. 13 of Chandre et al. 2003).

The lack of obvious evidence for chaos is particularly important for particles that migrate significantly in a short amount of time. To investigate this further, we looked at the orbits of the two particles in the top row of Fig. 7, which migrate ∼5 kpc in 0.5 Gyr. These two particles are chosen for their extreme rates of migration, where we may also expect to detect hints of non-linear effects. In the left-hand columns of the top two rows of Fig. 11 we show the orbits corotating with the faster, ∼65 km s^{-1} kpc^{-1} pattern, and in the middle panels the orbits are in the frame of the ∼40 km s^{-1} kpc^{-1} spiral. As in Fig. 9, the orbits are coloured according to the relative strength of the two spirals, whose amplitudes are shown in the bottom row. The radius as a function of time for each particle is shown as a black line in the rightmost column. Both particles cross the CR at almost the same time near the peak of the spiral amplitude, similar to the particles in Fig. 9. The two particles are first taken to the middle of the disc by the faster pattern and happen to be deposited near the CR and near the peak of the spiral pattern dominating there. They are therefore quickly taken further outward by this second, slower spiral. Thus, their rapid migration is simply due to two successive CRs. As before, the wavelet transform power spectrum shown in the rightmost column of Fig. 11 shows little evidence for significantly chaotic evolution.

We look further for signs of non-linearity by calculating the change in the Jacobi integral for a subset of the migrators. The Jacobi integral, $E_\mathrm{j} = E - \Omega_\mathrm{p} j_z$ is conserved in the rotating frame of a single, steady perturbation (Binney & Tremaine 2008). In our system we do not expect E_j to be exactly conserved anywhere since multiple patterns are always present in the disc, and the disc potential itself is constantly changing due to accretion of fresh gas and star formation. However, if single spirals are mostly responsible for instantaneous changes in j_z of individual stars, we would expect that for short time intervals the distribution of $\Delta E/\Delta j_z - \Omega_\mathrm{p}$ to be peaked and centred at zero for particles in the vicinity of each of the major CR regions. We select particles for these distributions by determining the $j_{z,\mathrm{CR}}$, i.e. the angular momentum of circular orbits at each CR, and then selecting the top 10 per cent of migrators with

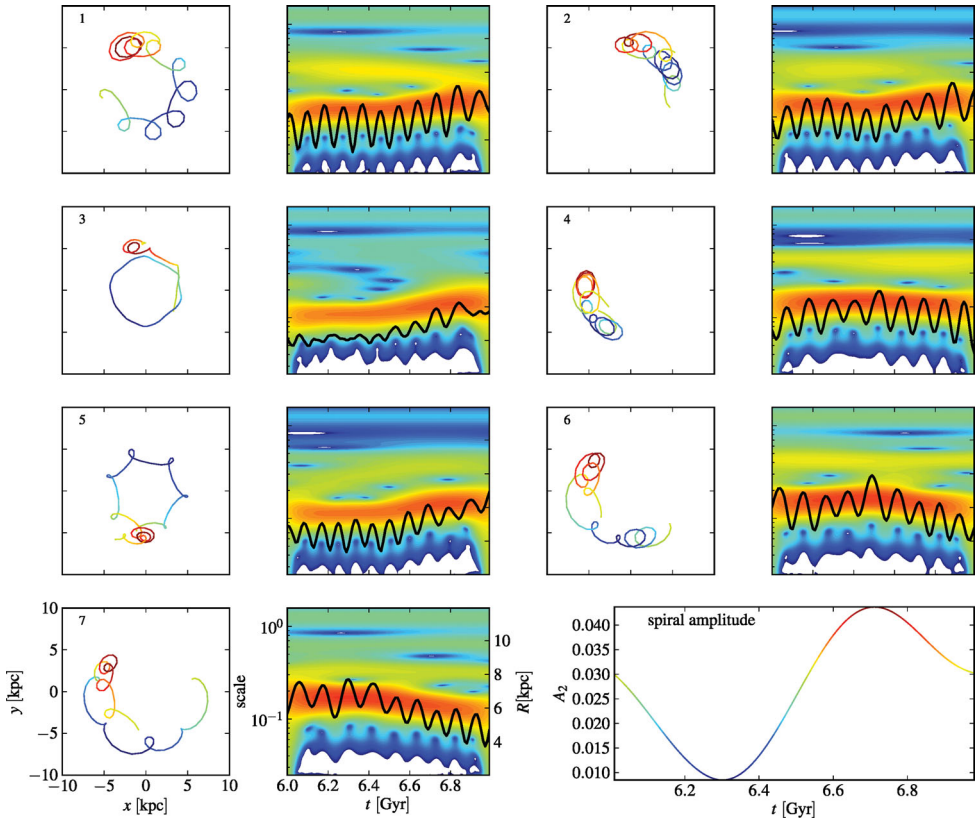

Figure 9. Columns 1 and 3: a selection of randomly selected orbits for a subsample of top 10 per cent of migrators on either side of the CR for the 43 km s^{-1} kpc^{-1} pattern in the time interval 6.5–7 Gyr. The orbits are in the frame corotating with the spiral. The colour corresponds to the relative spiral amplitude, as shown in the bottom right-hand panel. All boxes measure 20 kpc in x and y. The direction of rotation is counter-clockwise. Note that the time of CR crossing is easily identified as the orbit reverses direction. All CR crossings happen around the time of the spiral amplitude peak and are spatially correlated. Columns 2 and 4: the wavelet power spectrum of the x-component of the orbits is shown in colour contours. Note that most of the features are horizontal with few bends and vary smoothly, indicating lack of significant chaotic evolution. The solid black lines show the radius R in the x–y plane as a function of time. See the bottom left-hand panels for axis scales.

initial j_z within 10 per cent of $j_{z,\mathrm{CR}}$. In essence, we are selecting narrow strips of particles on either side of each CR line shown in Fig. 8. Note that we determined the pattern speeds in the 6.5–6.7 case separately from those determined in Fig. 4 and there is a slight discrepancy due to pattern speed evolution over Gyr time-scales.

The distributions for both time intervals are shown in Fig. 12. All distributions are centred near zero, within our uncertainties of pattern speed measurements of a few km s^{-1} kpc^{-1}. The distributions for the slower perturbations dominating in the outer disc are very strongly peaked, as expected if most of the particles are only being affected by a single spiral. The distributions for the faster perturbations are broadened for several reasons. First, the spiral amplitudes are variable which broadens their effective resonant frequencies. Secondly, in the inner disc other weaker patterns may be affecting the orbits. Still, it is striking that even in the 5.3–5.5 Gyr time interval, which was chosen specifically because multiple strong patterns are peaking at the same time (see also bottom panel of Fig. 10), the distributions do not appear qualitatively any different than for the quieter 6.5–6.7 Gyr time interval. The higher density of migrators seen in Fig. 10 could be due to several factors. First, the disc density is significantly higher at the CR of the 60 km s^{-1} kpc^{-1} spiral. The angular momentum exchange could further be facilitated by the presence of other perturbations, essentially feeding the CR of the dominant spiral. Nevertheless, even if the efficiency of migration is boosted due to the presence of other patterns, the fact that the distributions shown in Fig. 12 are centred and peaked at zero implies that the bulk of the angular momentum exchange still proceeds due to the CR of the individual spirals and that chaotic orbital evolution caused by the overlap of several resonances may not be the dominant cause of migration in this system. Note that the shift to the left from zero for the red distribution in the bottom panel of Fig. 12 is just a few km s^{-1} kpc^{-1} and therefore well within the measurement errors for Ω_p.

Similarly, we examine the evolution of E_j for the two particles shown in Fig. 11 that undergo very large migration over a short time interval. In the bottom right-hand panel we show the fractional changes in the Jacobi integral for these two particles. The fractional change for the faster pattern is measured with respect to the beginning of the time interval, whereas for the slower pattern we measure it with respect to the end of the interval (this is because initially the particles interact with the faster pattern and only later with the slower pattern). Between 5 and 5.6 Gyr, E_j in the frame of the 65 km s^{-1} kpc^{-1} pattern varies by <1 per cent. In the same time interval, the energy E (shown in red) and angular momentum (not shown for brevity) of these two particles change by 20 and 50 per cent, respectively. Between 5.6 and 6 Gyr, E_j in the frame of the $\sim$40 km s^{-1} kpc^{-1} pattern (blue lines) is again roughly constant, while energy and angular momentum continue to evolve and change by 30 per cent and a factor of 2.5 by the end of the time interval.

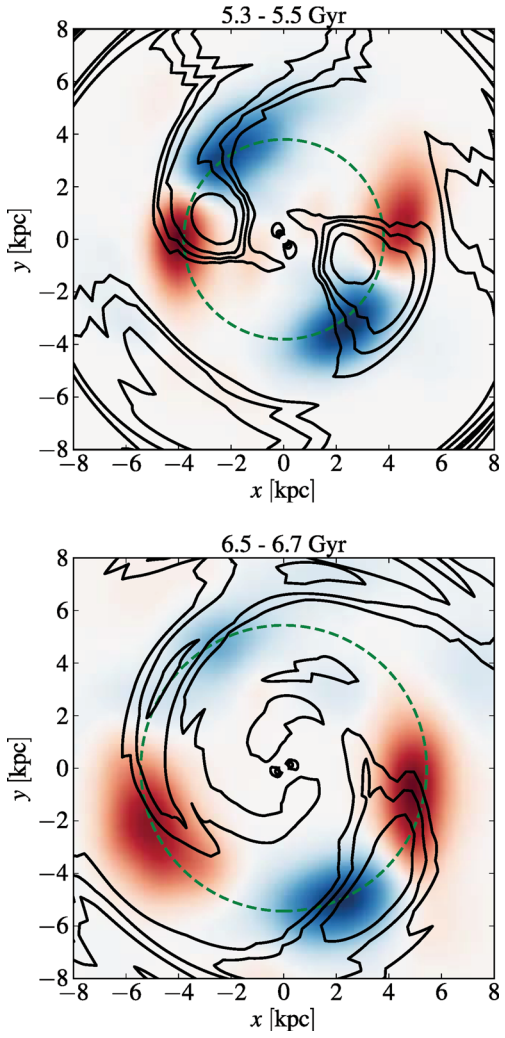

Figure 10. Density of particles migrating significantly in the time intervals 5.3–5.5 Gyr (top) and 6.5–6.7 Gyr (bottom). The sole selection criterion is that the particles are in the top 5 per cent in terms of their $|\Delta j_z|$ in the given time interval. The blue and the red colours show the outward and inward migrators, respectively. The black contours show the surface density of stars reconstructed from the $m = 2$ through $m = 4$ Fourier components. The dashed green circles mark the CR of the dominant pattern in the given time interval (65 km s^{-1} kpc^{-1} in the top panel and 45 km s^{-1} kpc^{-1} in the bottom). The direction of rotation is counter-clockwise.

4.2 Orbital circularity and migration

We now focus on the issue of orbital circularity and heating in CR migration. In Fig. 13, we show that the amount of angular momentum exchange is directly related to the circularity of an orbit. This is a crucial feature of corotation scattering, i.e. particles on the most circular orbits are also the most susceptible to having their orbits drastically altered. It follows that the largest changes in angular momentum are those that are essentially kinematically untraceable, because corotation scattering does not increase the random energy of an orbit appreciably (Lynden-Bell & Kalnajs 1972; SB02). Particles are selected in the same way as for Fig. 12 (for brevity, we only show the middle pattern that causes the largest amount of mixing). From the rotation curve and the midplane potential, we calculate the theoretical circular orbit locus in the (j, E) plane. Based on this locus we calculate the maximum allowable angular momentum, $j_c(E)$, of each particle based on its energy and express the circularity of its orbit as $j_z/j_c(E)$.

We calculate the mass weighted distribution of $|\Delta j_z|$ as a function of $x \equiv j_z/j_c(E)$ which can be expressed as

$$f(x) = \sum_{i=1}^{N} |\Delta j_{z,i}| m_i \delta(x - x_i), \tag{4}$$

where the subscript i indicates individual particle quantities, m is the mass and N is the total number of particles. The corresponding cumulative distribution function is given by

$$F(x) = \frac{\sum_{\eta=0}^{\eta=x} f(\eta)}{\sum_{\eta=0}^{\eta=1} f(\eta)} \tag{5}$$

and shown in Fig. 13. Note that even for particles on fairly eccentric orbits, changes in j_z are possible, but those are most likely occurring at the Lindblad resonances. However, the contribution of those stars to the overall changes in j_z is miniscule. The particles with $j_z/j_c(E) > 0.95$ account for over 50 per cent of the angular momentum exchange. This follows since $|\Delta j_z|$ is largest for those particles, but also simply due to the fact that the disc is kinematically cool and particles on mostly circular orbits are also most abundant. However, the mass distribution (shown by the dashed line in the same panel) is much less peaked than the angular momentum distribution, confirming that particles on circular orbits are most important for the exchange of angular momentum.

Apart from being most efficient at relocating particles on the most circular orbits, SB02 also showed that CR scattering also does not appreciably heat the disc. In Fig. 14 we show a probability density distribution of $\Delta[j_z/j_c(E)]$ given ΔR over the same time interval studied in Figs 8 and 12. Positive values of $\Delta[j_z/j_c(E)]$ indicate an *increase* in circularity or a 'cooling' of the orbit, while negative values correspond to heating. The majority of the particles that migrate outwards suffer very minor heating, while the inward-migrating particles heat slightly more. The particles moving the farthest outward also get heated the *least* on average – this is the key feature of CR scattering because it allows particles to experience multiple scatterings, thereby allowing for potentially very large changes in radius during their lifetimes. Interestingly, roughly 10 per cent of the particles that migrate outward have their orbits cooled by the spiral.

Note from the top panel of Fig. 8 that the most obvious and dramatic feature in Δj_z versus j_z occurs due to a resonance with the 43 km s^{-1} kpc^{-1} pattern that does not appear dominant in Fig. 5. The ∼20 km s^{-1} kpc^{-1} spiral that dominates the power spectrum on the other hand causes relatively little mixing. Determining the dominance of patterns from Fig. 4 is somewhat misleading because the power spectrum is constructed using the normalized Fourier coefficients. Thus, although the slowest pattern appears to dominate, it peaks in the far outer disc where the density is low and therefore the perturbation does not involve much mass. The middle pattern instead is also at an optimal point in the disc. The dashed line in Fig. 1 shows the Toomre Q parameter at 8 Gyr, which is near the interval we have been analysing. In the inner disc where the fast pattern CR occurs, Toomre Q approaches values of 4 and above – similarly in the outer disc, where the slow pattern CR occurs Q increases rapidly and the disc density is very low (the break occurs at ∼8 kpc but the CR is at ∼11 kpc). For the middle pattern CR, Q is relatively low while the disc density on the other hand is still reasonably high. Therefore the CR is well populated by kinematically cool stars and the middle pattern can achieve the most mixing.

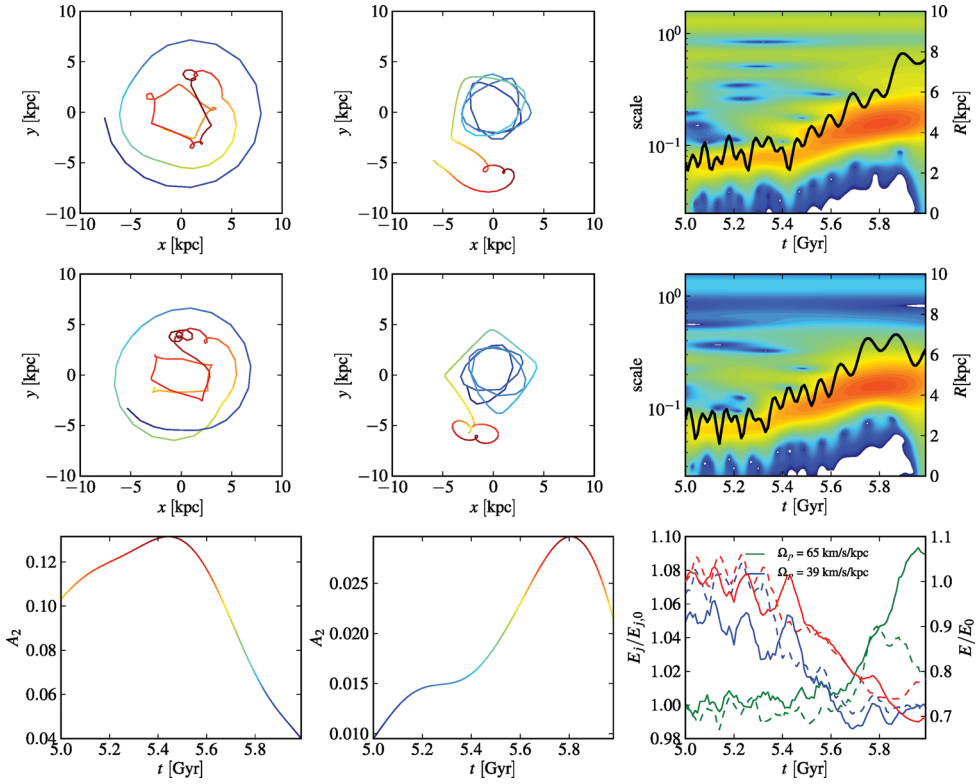

Figure 11. Columns 1 and 2: similar to Fig. 9 but for the two orbits shown in the top row of Fig. 7. The orbits are in the frame corotating with the inner spiral (column 1) and the mid-disc spiral (column 2) in the time interval 5–6 Gyr, when they happen to migrate substantially. The colour corresponds to the relative spiral amplitude, as shown in the bottom row. All boxes measure 20 kpc in x and y. The direction of rotation is counter-clockwise. Note that the time of CR crossing is easily identified as the orbit reverses direction. Column 3: the top two rows show the wavelet power spectrum of the x-component of the orbits in colour contours. The solid black lines show the radius R in the x–y plane as a function of time. The bottom panel in column 3 shows the fractional time evolution of the Jacobi constant, E_j, in the frame of the two spirals (green and blue lines correspond to the 65 and 39 km s^{-1} kpc^{-1} patterns, respectively) and energy, E (red lines). Because of different ranges of values, the left- and right-hand y-axes are used for E_j and E, respectively. Particles 1 and 2 are shown in solid and dashed lines. When the particles are in the corotation region of a given pattern, E_j is conserved to ∼1 per cent, while E evolves by 30 per cent (though not shown, angular momentum changes by a factor of 2.5).

5 NUMERICAL TESTS

Spiral arms are amplified disturbances in discs, but the source of the seed perturbation is not well understood. It is often assumed that in isolated discs, the seed is noise in the density distribution (e.g. Goldreich & Lynden-Bell 1965). In simulations like the ones presented here, the natural source of noise is the finite particle numbers, which are in general several orders of magnitude smaller than the number of stars in real galactic discs, though in real galaxies giant molecular clouds are a similar source of 'noise'. Numerical resolution studies abound in the literature, but most often attention has been given to the requirements of collisionless cosmological simulations to resolve DM substructure (e.g. Moore et al. 1998). In the cases where disc secular evolution has been addressed specifically, most resolution studies have addressed the resonant couplings between DM haloes and bars, but again most often only collisionless simulations were used (e.g. Debattista & Sellwood 2000; Valenzuela & Klypin 2003; Holley-Bockelmann, Weinberg & Katz 2005; Weinberg & Katz 2007; Dubinski, Berentzen & Shlosman 2009). Spiral structure and in particular SPH simulations in isolation are addressed less often, though recently Christensen et al. (2010) presented a global disc resolution study focusing mostly on the resolution dependence of subgrid star formation and feedback prescriptions. Unfortunately, their high-resolution runs use approximately the same resolution as the fiducial runs here, because their work was meant as a guide for cosmological simulations where the state-of-the-art uses comparable or slightly lower resolution. Their results therefore cannot be used to ascertain the validity of our results.

In this section, we discuss several numerical tests to explore the robustness and variability of the spiral activity presented in the preceding sections. The main concern here is that the resulting spirals may be dependent on the Poisson particle noise for their generation and subsequent evolution. We performed runs with 0.5, 2 and 4 times the fiducial particle number of 10^6 particles per component in the initial conditions. Softened gravity could be particularly relevant to discs because it can potentially set the relevant perturbation scales. We therefore ran several simulations with different choices for the softening length. A possible source of numerical heating of the disc is massive DM particles, so we also ran a simulation with an order of magnitude more DM particles. We discuss each of these in turn below.

5.1 Stochasticity

Sellwood & Debattista (2009) examined the effects of stochasticity on the growth and pattern speed evolution of bars. They found that small perturbations in the initial conditions could lead to divergent behaviour, independent of the code used for the integration. Spirals result from amplified disturbances and are intrinsically sensitive to

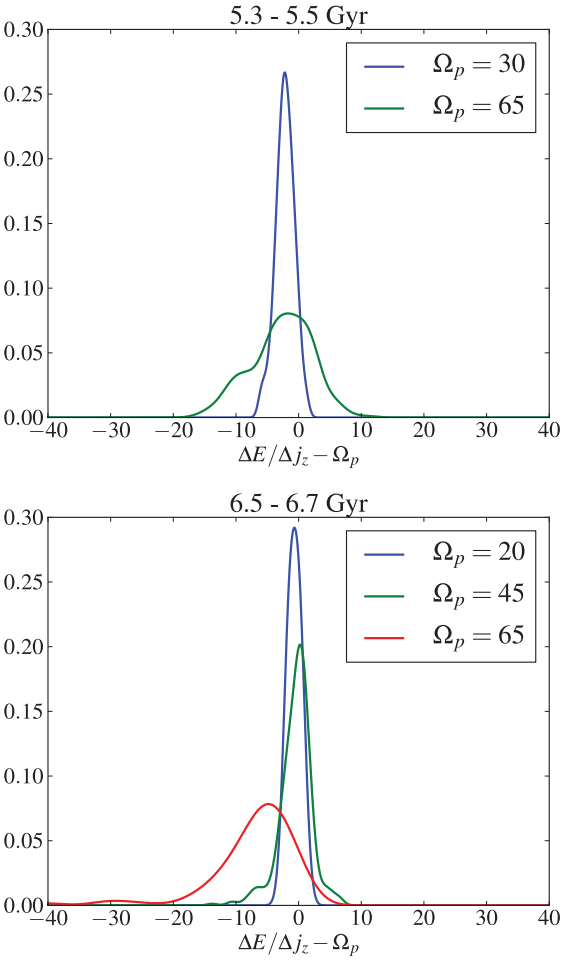

Figure 12. Distributions of $\Delta E/\Delta J_z - \Omega_p$ for particles with the largest changes in J_z near the CRs of patterns identified from the Fourier analysis. The top and bottom panels show the 5.3–5.5 and 6.5–6.7 Gyr time intervals, respectively.

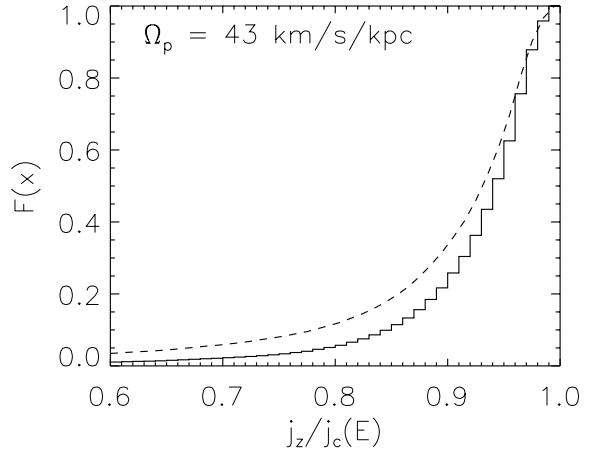

Figure 13. Cumulative distribution of $j_z/j_c(E)$ weighted by $|\Delta j_z|$ – see equations (4) and (5) for a description of $F(x)$. The dashed line shows the cumulative distribution of $j_z/j_c(E)$.

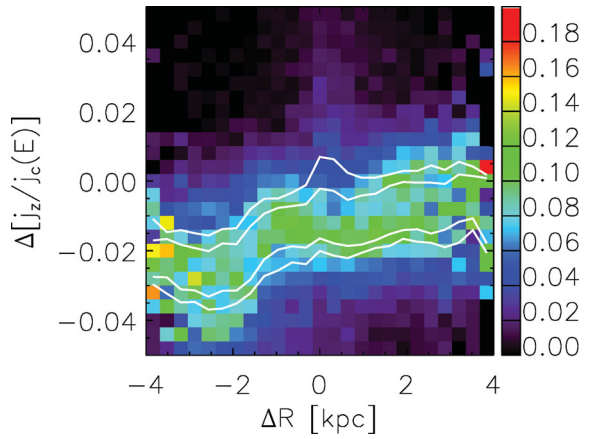

Figure 14. Probability distribution of the change in the ratio of $j_z/j_c(E)$ for the same particles used to construct the green distribution in the top panel of Fig. 12 and in Fig. 13, interacting with the 42 km s^{-1} kpc^{-1} pattern over the 6.5–7 Gyr time interval. The inner (outer) white contours enclose 50 per cent (75 per cent) of the mass in each ΔR bin. Values are normalized such that in the vertical direction, $\sum P \mathrm{d}A = 1$, where dA is the area of the bin.

stochastic effects. It is therefore not possible to expect the pattern speed and amplitude evolution to match exactly among the different runs. To get some sense of the natural range of behaviour due to stochasticity, we ran two simulations with identical numerical parameters and initial conditions, but we altered the random seed used in the generation of initial particle positions sampled from the distribution function. The general disc properties that result from 10 Gyr of evolution are very similar, with inner scale lengths ranging from 3.1 to 3.3 kpc.[4]

In Fig. 15 we show the evolution of the $m = 2$ Fourier amplitude at four different radii in the disc for all runs. We show smoothed $m = 2$ time series because otherwise the rapid oscillations of the amplitudes make it difficult to discern their overall evolution. The colours represent the amplitude at different radii. Bar/oval growth can be identified in this representation whenever the black and blue lines grow together. The middle and right-hand panels of the top row show the stochasticity test runs (fiducial, T2 and T3) – apparently the timing of the growth of spirals is very different between the three runs with different random seeds. Run T2 does not grow a central oval at all (the black and blue lines showing 2 and 4 kpc are almost completely featureless), whereas the fiducial run and run T3 both have episodes of bar/oval formation. In the fiducial run, this occurs at ∼3, 4 and 6 Gyr, whereas for the T3 run it occurs at 3 and 6 Gyr. In Fig. 16 we show the pattern speed evolution derived in the same way as in Fig. 5 with the panels corresponding to panels in Fig. 15. Very similar pattern speeds occur in all three discs, as shown by the top row of Fig. 16. For example, the same outer (slow) pattern can be seen in the three power spectra, starting at around 30 km s^{-1} kpc^{-1} and slowly decaying to 20 km s^{-1} kpc^{-1} by 10 Gyr. The pattern speeds are qualitatively similar in all runs and presumably depend upon the overall disc structure, which is relatively robust against stochastic effects. The amplitude and timing of the spirals, on the other hand, may vary considerably.

5.2 Softening

The second row of Fig. 15 shows the time evolution of the $m = 2$ perturbations at four different radii for the runs with different

[4] These values were obtained using fits to surface density profiles. If we instead fit midplane volume-density profiles, the resulting scale lengths are ∼2.5 kpc, in agreement with Jurić et al. (2008) values obtained for the MW from SDSS data.

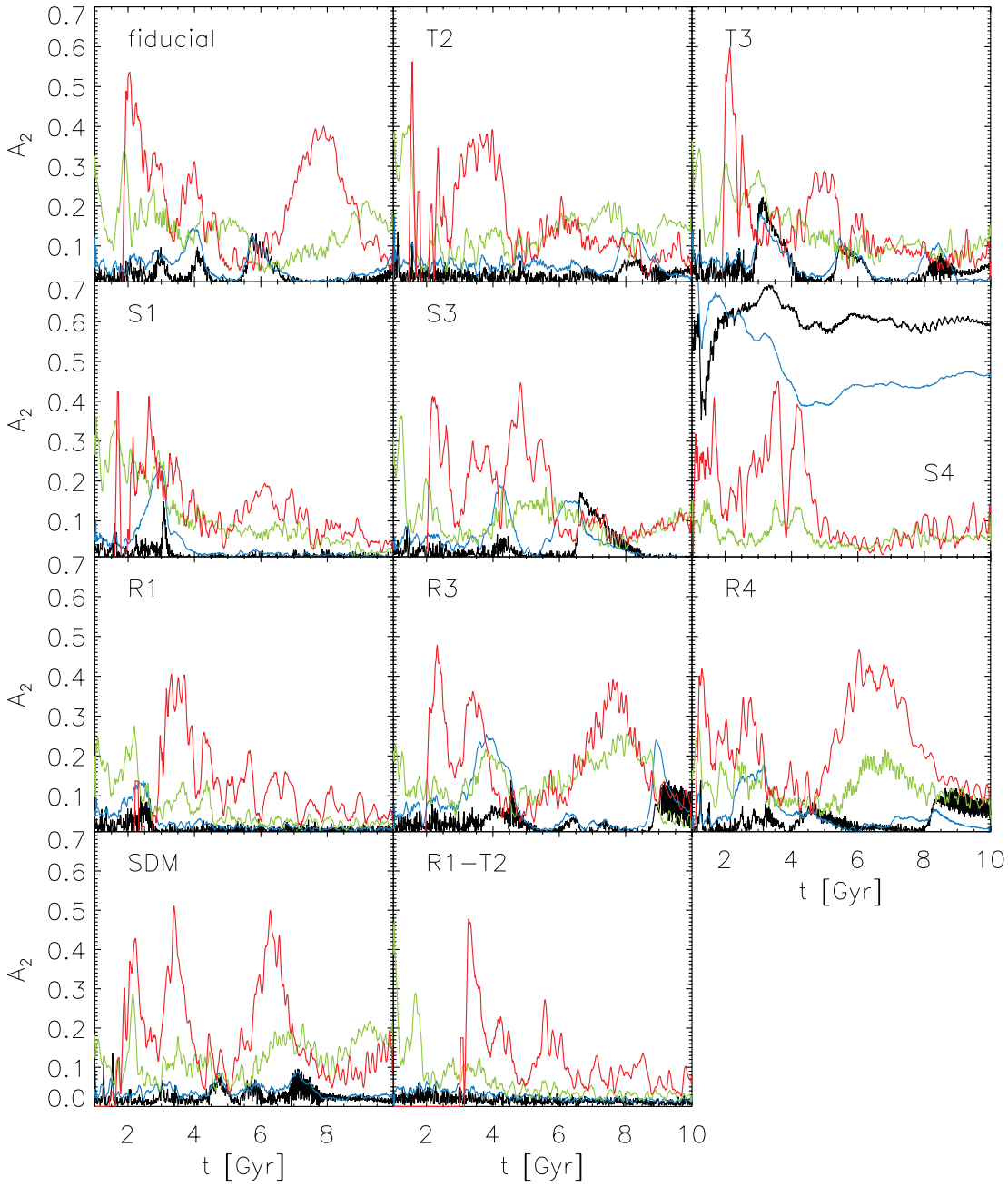

Figure 15. Fourier amplitudes as a function of time for the entire suite. The fiducial run is shown in upper left, followed by the stochasticity tests in the same row. Second row shows runs with different softenings; the third row shows runs with different particle numbers. Bottom row shows runs SDM and R1-T2. Different colour lines represent the amplitude at different radii – black, blue, green and red correspond to 2, 4, 8 and 12 kpc respectively.

values of the softening parameter. This suggests that the simulations with $h_s \leq 100$ pc yield qualitatively similar spiral structure, though S1 (leftmost panel) harbours somewhat more damped spirals, especially mid-disc (green line). Run S4 is clearly wildly different, developing a large and persistent bar very early (in subsequent discussions we ignore this run). This comparison shows significant variance in the timing of spiral activity, but the amplitudes at different radii for runs S1 and S3 appear very similar to the fiducial run (upper left-hand panel). The second row of Fig. 16 shows the corresponding pattern speed evolution and confirms that for runs S1 and S3, the pattern speeds supported by the disc are very similar to each other and to the fiducial run.

5.3 Particle number

The third row of Figs 15 and 16 shows the $m = 2$ amplitude and pattern speed evolution for runs R1, R3 and R4 (0.5, 2 and 4 times the fiducial particle number, respectively). Run R1 stands out in this comparison, as the structure that develops is significantly weaker. We investigated whether this is a manifestation of stochasticity and ran a second simulation where the initial conditions were generated using a different random seed (run R1-T2). The results are shown in the right-hand panel of the bottom row – the evolution of this experiment is essentially identical to R1, suggesting that the weaker structure is not a stochastic effect.

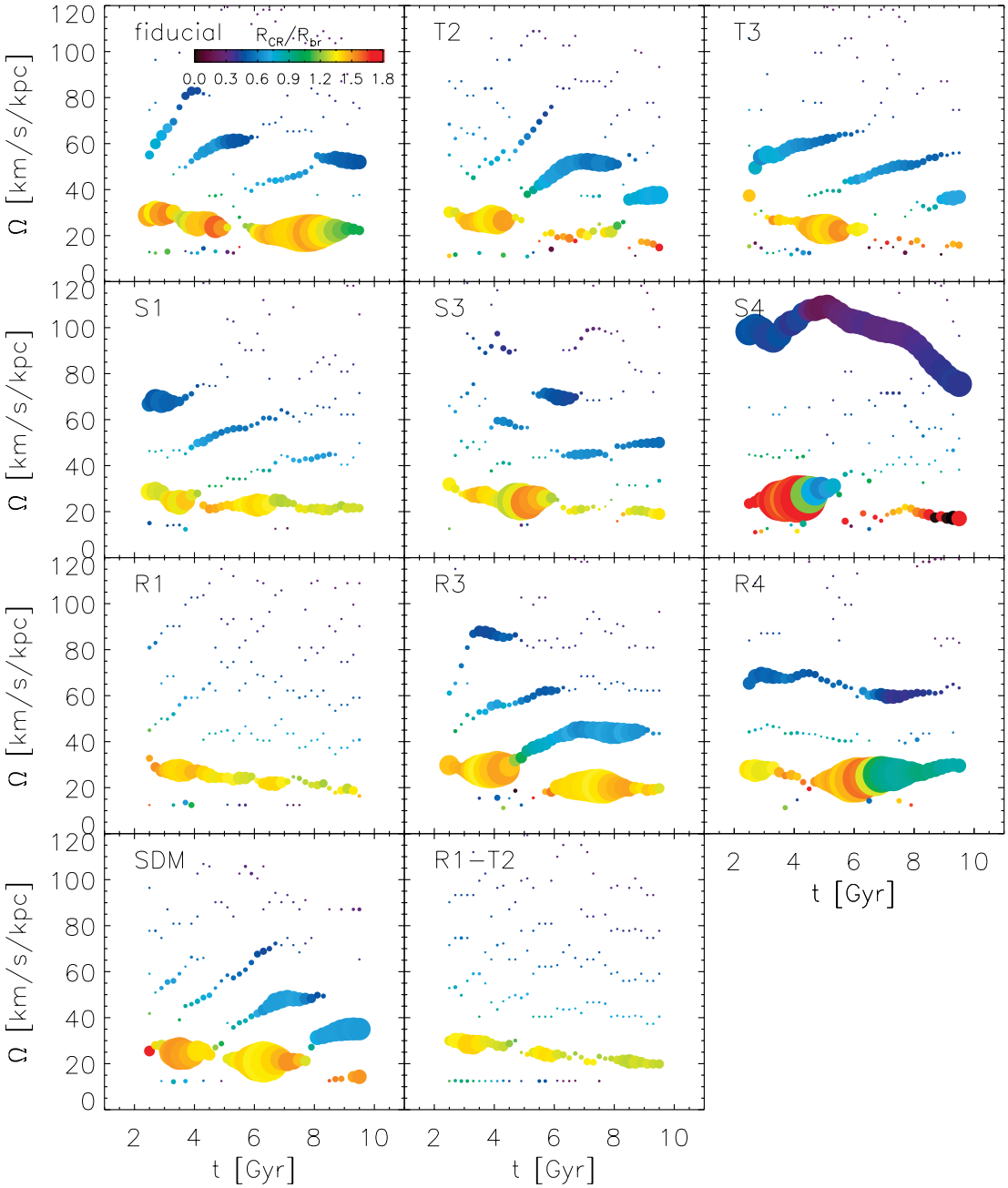

Figure 16. Pattern speed evolution as a function of time. Colours and point sizes are as in Fig. 5. Panels correspond to panels from Fig. 15.

The star formation rates are the same in all four runs. As a result, the discs are composed of proportionally similar amounts of stars – roughly 2, 1, 4 and 8 million for the fiducial, R1, R3 and R4 runs, respectively.

In runs R3 and R4, the structure is much more similar to the fiducial run. The timing of perturbation growth is slightly different, but the frequencies are essentially the same for all four runs. The consistency of these results affirms that the runs in our simulation suite have sufficient numbers of particles to adequately model the disc dynamics. Ideally, we would be able to perform simulations with still higher particle numbers to truly test for convergence, but due to computational cost such simulations were not feasible at this time.

The ratio of CR to the break radius (i.e. the colour of the points) for the $\sim$30 km s^{-1} kpc^{-1} pattern in run R4 appears different from $t \sim 6.5$ Gyr onwards. These differences are not particularly drastic, however, and the relative locations of the CR are consistent. The speeds of the main patterns are similar to the runs in the top row (fiducial, T1, T2). We also see an even slower pattern, probably due to increased particle numbers, which make its detection in the far outer disc possible.

Finally, because DM particles are constantly bombarding the disc, we explored the possibility that their perturbations may influence the generation of spirals. In the bottom left-hand panel of Fig. 15, we show the $m = 2$ amplitude for run SDM, which was initialized with 10 times as many DM particles. Other properties of the run

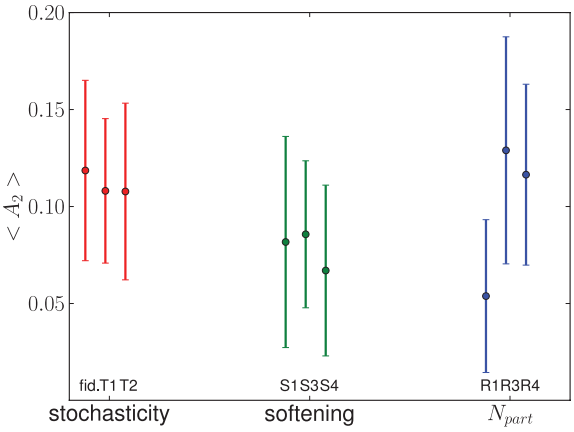

Figure 17. The mean $m = 2$ amplitude over the whole simulation for all of the runs in our suite. The error bars indicate the standard deviation. Points are offset horizontally for readability.

were kept the same as in the fiducial run. Spiral amplitudes are very similar to the fiducial run, although the innermost pattern seems to be missing. In the corresponding panel in Fig. 16 the frequencies as a function of time for the run SDM appear very similar to the fiducial run. At most times, the dominant frequencies present in both discs are essentially the same.

While we have achieved convergence with increasing mass resolution, the discrepancy between our lowest resolution run, R1, and the rest of the suite is puzzling. We tested for the effect of two-body relaxation by increasing the softening and by increasing the number of particles in the DM halo. We also tested for potential integration issues stemming from different softenings between the baryons and the DM (note that in all of our runs the DM and baryons use different softening, and this is standard practice in such simulations). Making the baryon softening equal to the DM softening was the only experiment that yielded results more in line with other runs.

5.4 Overall comparison

In the preceding subsections we investigated the detailed evolution of spirals in our simulation suite, but how do these simulations compare in their global properties? In Fig. 17 we show the mean $m = 2$ amplitude, $\langle A_2 \rangle$, calculated over the duration of the entire simulation, and its standard deviation represented by the error bars. Stochasticity and choice of softening minimally impact the global disc evolution, though all of the S-series runs have slightly smaller $\langle A_2 \rangle$, especially S4. A true outlier is R1, with lower $\langle A_2 \rangle$ than the rest of the suite.

The properties of spirals are important in our understanding of radial migration because of their effect on the distribution of stars in the disc. We have seen in Figs 15 and 16 that while the range of admissible pattern speeds is not sensitive to choices of numerical parameters, the timing of the spirals can differ substantially. Depending on the configuration of the disc, this could affect the migration rates and ultimately the predictions we extract from these models for studies of disc stellar populations. It is difficult to quantitatively assess the spiral structure, though we have attempted to do so in Fig. 17 and found no appreciable differences in the suite apart from run R1. However, we can quantitatively analyse the properties of resulting stellar populations in a given region of the disc.

A natural region to examine is the model analogue to the solar neighbourhood. In the top panels of Fig. 18 we show the distributions of formation radii for stars that are found within $7 < R\,(\mathrm{kpc}) < 9$ at the end of the simulation. This choice is particularly important because we have addressed this same region in our previous works (R08b; Loebman et al. 2011). The bottom panels show the corresponding cumulative distributions. The solid black line in all panels corresponds to the fiducial run – the left-hand, middle and right-hand columns show the stochasticity, softening and resolution tests, respectively.

The leftmost panels show that stochasticity has little overall effect on the cumulative distributions of R_{form} – at 50 per cent the difference is $\leq$0.5 kpc. Nevertheless, the distribution in the top panel shows that the fiducial run may even overproduce the in situ stars.

In the remaining cumulative distributions, the overall variance at 50 per cent does not exceed that of the stochasticity tests. Two notable cases are apparent – the run S1 and run SDM. Run S1, is more heavily dominated by in situ stars. This agrees with the fact that this run develops weaker spiral structure in the final Gyr. However, the appearance of the larger peak of in situ stars for the run S1 may also simply be another manifestation of stochasticity – when we recreate the same distributions 2 Gyr earlier, the run S1 follows almost exactly the fiducial distribution.

For run SDM, the peak of the R_{form} distribution is actually shifted away from the solar neighbourhood. This implies even more drastic mixing, and is indeed also apparent when we repeat the experiment at 8 Gyr (as mentioned in the previous paragraph). Regardless of these subtle variations, the fact that >50 per cent of solar neighbourhood stars originated in other parts of the disc remain robust.

Contrary to what we might expect for run R1 given Figs 15–17, where we found that it has weaker spiral structure on average from other runs, we find here only a small difference in the solar neighbourhood population. We would expect the resultant migration to be much less than in the other runs. We therefore studied the spiral structure in this run in more detail and found that while the disc does not support strong spirals, it is permeated with weaker and highly transient features. We find that the transience is much more pronounced than in the other runs. Using a 1-Gyr baseline power spectrum, as in Fig. 4, we find essentially a continuous spectrum of patterns emerges, compared with few distinct features. This is apparent also in Fig. 16, where many weak patterns at a variety of pattern speeds are identified. The pattern speeds shift on short timescales, allowing even the weak structure to relatively efficiently redistribute the stars.

6 CONCLUSIONS

Radial migration is rapidly becoming recognized as a critical process in disc galaxies because of its wide-ranging implications. If this process has been important for the MW, it most likely played a key role in determining the mix of stars in the solar neighbourhood today (SB02; R08a,b; Schönrich & Binney 2009a,b; Minchev & Famaey 2010; Lee et al. 2011; Loebman et al. 2011; Bird, Kazantzidis & Weinberg 2012). On a broader scale, it has likely influenced the stellar population gradients measured in the MW disc and other galaxies (Boissier & Prantzos 2000; MacArthur et al. 2004; R08b; Williams et al. 2009; Gogarten et al. 2010; Muñoz Mateos et al. 2011; Vlajić, Bland-Hawthorn & Freeman 2011), and contributed substantially to the stellar density in the outermost disc regions (Barker et al. 2007, 2011; de Jong et al. 2007; Azzollini et al. 2008; Bakos et al. 2008; R08a; Roškar et al. 2010; Yoachim et al. 2010, 2012; Alberts et al. 2011).

In this paper, we have investigated in detail the origin of radial migration by analysing the spontaneously forming spiral structure and the resultant resonant angular momentum exchange. We found

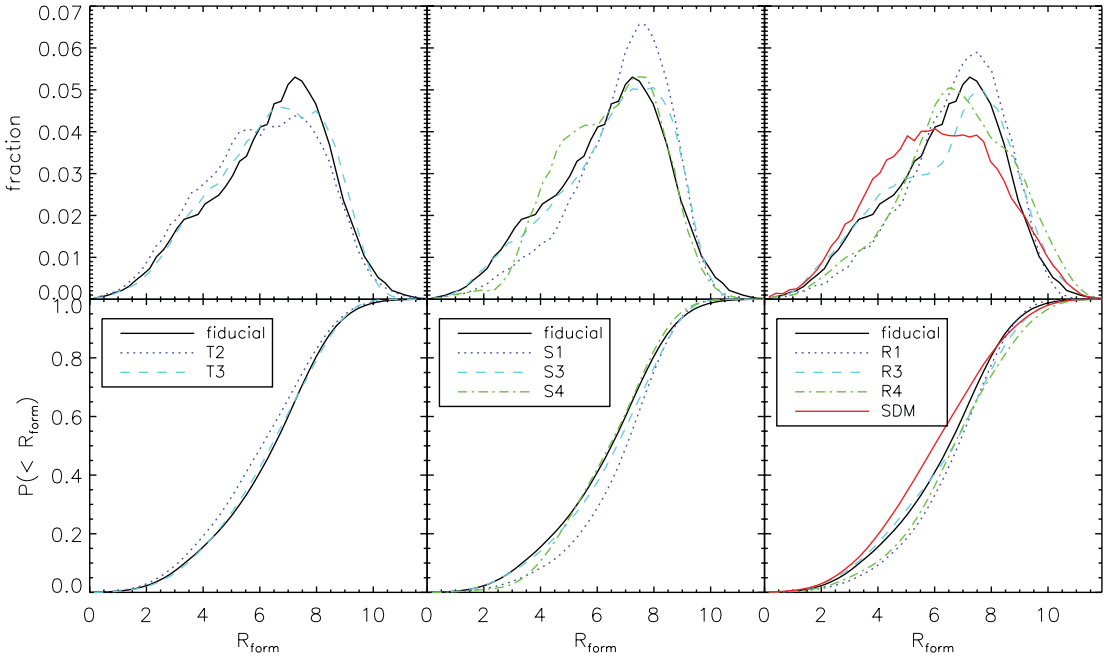

Figure 18. Top: histograms of $R_{\rm form}$ for particles with $7 < R_{\rm final}$ (kpc) < 9. Bottom: corresponding cumulative distribution functions.

that the spiral structure is transient in amplitude, but appears to support only a few discrete pattern speeds at any given time. This means that some stars can be tossed from the CR of one pattern to another, resulting in large changes in radius on relatively short time-scales. Still, it is important to remember that extreme migrations of many kpc over the course of a star's lifetime are not the norm, they comprise the tail of the distribution. This can be seen in Fig. 18 – although ∼50 per cent of the stars do come from elsewhere, this also means that the near-majority have formed in situ. The situation changes with increasing radius, because the in situ star formation decreases – thus, the tail of the distribution from the inner regions makes up the majority of the stellar population at large radii.

We demonstrated in Section 4 that the largest angular momentum exchanges occur at the corotation of important $m = 2$ spirals. An important aspect of our result is the confirmation that the largest angular momentum exchange happens for particles on the most circular orbits – and that these particles do not get heated by the spirals while they migrate (SB02). This is a crucial aspect of the CR migration mechanism because it means that the process is not self-limiting. Instead, it can continue especially for the particles migrating the most, allowing for very large changes in radius for some of the stars, but without betraying their journey by anomalous kinematics. We have also searched for signs of chaotic orbital evolution in the vicinity of resonances, but found indication that stellar orbits remain rather regular as they migrate radially. We have found this to be the case even for very large migrations, and have shown that such migrations are possible in a short amount of time if a particle passes directly from the CR of one spiral to another (see Figs 9 and 11).

Our results show that the redistribution of stars in MW-type discs on very short time-scales is inevitable if transient spiral structure is present. Even in the case of run R1, where the mid-disc spirals appear to be numerically suppressed, a large fraction of stars ending up in the solar neighbourhood originated in the interior of the disc. Therefore, our findings suggest that the effects of recurring, spontaneous spiral structure are a key component of disc evolution that models simply *must* include if they wish to make predictions about kinematic and chemical properties of stellar populations. Cosmological simulations which fail to form discs that can support spiral structure may be missing critical aspects of disc evolution and therefore the detailed properties of resulting disc stellar populations must be used with care. On the other hand, the inclusion of substructure (e.g. Bird et al. 2012) is important not only because mergers can heat and disrupt the disc, but also because they may trigger transient structure. We hope that it should soon be possible to use state-of-the-art cosmological simulations (e.g. Agertz, Teyssier & Moore 2011; Guedes et al. 2011) for detailed studies of radial migration.

ACKNOWLEDGMENTS

We wish to thank the anonymous referee for constructive comments that greatly enhanced the paper. RR was supported in part by the NSF ITR grant PHY 02-05413 (also partially supporting TRQ), the NASA AISR grant NNX08AD19G, the Forschungskredit grant at the University of Zürich, and the Marie curie International Reintegration Grant. Simulations used in this study were performed on a cluster purchased in part by a grant from the University of Washington Student Technology Fee, on resources provided by the TereaGrid (in particular Lonestar and Ranger at the Texas Advanced Computing Centre and Kraken at the National Institute for Computational Sciences), and on the Schrödinger supercomputer at the University of Zürich.

REFERENCES

Agertz O., Teyssier R., Moore B., 2011, MNRAS, 410, 1391
Alberts S. et al., 2011, ApJ, 731, 28
Azzollini R., Trujillo I., Beckman J., 2008, ApJ, 679, L69
Bakos J., Trujillo I., Pohlen M., 2008, ApJ, 683, L103
Barbanis B., Woltjer L., 1967, ApJ, 150, 461
Barker M., Sarajedini A., Geisler D., Harding P., Schommer R., 2007, AJ, 133, 1125

Barker M. K., Ferguson A. M. N., Cole A. A., Ibata R., Irwin M., Lewis G. F., Smecker-Hane T. A., Tanvir N. R., 2011, MNRAS, 410, 504
Binney J., Lacey C., 1988, MNRAS, 230, 597
Binney J., Tremaine S., 2008, Galactic Dynamics, 2nd edn. Princeton Univ. Press, Princeton, NJ
Bird J. C., Kazantzidis S., Weinberg D. H., 2012, MNRAS, 420, 913
Bland-Hawthorn J., Krumholz M., Freeman K., 2010, ApJ, 713, 166
Boissier S., Prantzos N., 1999, MNRAS, 307, 857
Boissier S., Prantzos N., 2000, MNRAS, 312, 398
Brooks A., Governato F., Quinn T., Brook C., Wadsley J., 2009, ApJ, 694, 396
Brunetti M., Chiappini C., Pfenniger D., 2011, A&A, 534, 75
Bullock J., Dekel A., Kolatt T., Kravtsov A., Klypin A., Porciani C., Primack J., 2001, ApJ, 555, 240
Chandre C., Wiggins S., Uzer T., 2003, Physica D, 181, 171
Chiappini C., Matteucci F., Romano D., 2001, ApJ, 554, 1044
Christensen C. R., Quinn T., Stinson G., Bellovary J., Wadsley J., 2010, ApJ, 717, 121
Daubechies I., 1990, IEEE Trans. Inf. Theory, 36, 961
Debattista V., Sellwood J., 2000, ApJ, 543, 704
Debattista V., Mayer L., Carollo C., Moore B., Wadsley J., Quinn T., 2006, ApJ, 645, 209
de Jong R. et al., 2007, ApJ, 667, L49
de Jong J. T. A., Yanny B., Rix H.-W., Dolphin A. E., Martin N. F., Beers T. C., 2010, ApJ, 714, 663
Dubinski J., Berentzen I., Shlosman I., 2009, ApJ, 697, 293
Freeman K., Bland-Hawthorn J., 2002, ARA&A, 40, 487
Freeman K., Bland-Hawthorn J., 2008, in Kodama T., Yamada T., Aoki K., eds, ASP Conf. Ser. Vol. 399, Panoramic Views of Galaxy Formation and Evolution. Astron. Soc. Pac., San Francisco, p. 439
Gemmeke J., Portegies Zwart S., Kruip C., 2008, Commun. Nonlinear Sci. Numer. Simulation, 13, 1157
Gogarten S. et al., 2010, ApJ, 712, 858
Goldreich P., Lynden Bell D., 1965, MNRAS, 130, 125
Guedes J., Callegari S., Madau P., Mayer L., 2011, ApJ, 742, 76
Holley-Bockelmann K., Weinberg M., Katz N., 2005, MNRAS, 363, 991
Holmberg J., Nordström B., Andersen J., 2009, A&A, 501, 941
Ivezić Ž. et al., 2008, ApJ, 684, 287
Jenkins A., Binney J., 1990, MNRAS, 245, 305
Jurić M. et al., 2008, ApJ, 673, 864
Kaufmann T., Mayer L., Wadsley J., Stadel J., Moore B., 2006, MNRAS, 370, 1612
Kaufmann T., Mayer L., Wadsley J., Stadel J., Moore B., 2007, MNRAS, 375, 53
Kazantzidis S., Magorrian J., Moore B., 2004, ApJ, 601, 37
Kazantzidis S., Bullock J., Zentner A., Kravtsov A., Moustakas L., 2008, ApJ, 688, 254
Kereš D., Katz N., Weinberg D., Davé R., 2005, MNRAS, 363, 2
Lee Y. S. et al., 2011, ApJ, 738, 187
Lepine J. R. D., Acharova I. A., Mishurov Y. N., 2003, ApJ, 589, 210
Loebman S. R., Roškar R., Debattista V. P., Ivezić Ž., Quinn T. R., Wadsley J., 2011, ApJ, 737, 8
LSST Science Collaborations, 2009, (arXiv:0912.0201)
Lynden Bell D., Kalnajs A., 1972, MNRAS, 157, 1
MacArthur L., Courteau S., Bell E., Holtzman J., 2004, ApJS, 152, 175
Macciò A. V., Dutton A. A., van den Bosch F. C., Moore B., Potter D., Stadel J., 2007, MNRAS, 378, 55
Matteucci F., Francois P., 1989, MNRAS, 239, 885
Miller G. E., Scalo J. M., 1979, ApJS, 41, 513
Minchev I., Famaey B., 2010, ApJ, 722, 112
Minchev I., Famaey B., Combes F., Di Matteo P., Mouhcine M., Wozniak H., 2011, A&A, 527, A147
Minchev I., Famaey B., Quillen A. C., Di Matteo P., Combes F., Vlajic M., Erwin P., Bland-Hawthorn J., 2012, arXiv e-prints (arXiv:1203.2621)
Moore B., Governato F., Quinn T., Stadel J., Lake G., 1998, ApJ, 499, L5
Muñoz Mateos J. C., Boissier S., Gil de Paz A., Zamorano J., Kennicutt J., Moustakas J., Prantzos N., Gallego J., 2011, ApJ, 731, 10
Navarro J. F., Frenk C. S., White S. D. M., 1997, ApJ, 490, 493
Nener B., Ridsdill-Smith T., Zeisse C., 1999, Infrared Phys. Technol., 40, 399
Perryman M. A. C. et al., 2001, A&A, 369, 339
Press W. H., Teukolsky S. A., Vetterling W. T., Flannery B. P., 1992, Numerical Recipes in C. The art of scientific computing. Cambridge Univ. Press, Cambridge
Prieto C. A. et al., 2008, Astron. Nachr., 329, 1018
Quillen A. C., 2003, AJ, 125, 785
Radburn-Smith D. J. et al., 2012, ApJ, 753, 138
Rix H.-W., Zaritsky D., 1995, ApJ, 447, 82
Roškar R., Debattista V., Stinson G., Quinn T., Kaufmann T., Wadsley J., 2008a, ApJ, 675, L65 (R08a)
Roškar R., Debattista V., Quinn T., Stinson G., Wadsley J., 2008b, ApJ, 684, L79 (R08b)
Roškar R., Debattista V. P., Brooks A. M., Quinn T. R., Brook C. B., Governato F., Dalcanton J. J., Wadsley J., 2010, MNRAS, 408, 783
Ruchti G. R. et al., 2011, ApJ, 737, 9
Schönrich R., Binney J., 2009a, MNRAS, 396, 203
Schönrich R., Binney J., 2009b, MNRAS, 399, 1145
Sellwood J. A., Athanassoula E., 1986, MNRAS, 221, 195
Sellwood J., Binney J., 2002, MNRAS, 336, 785 (SB02)
Sellwood J. A., Carlberg R. G., 1984, ApJ, 282, 61
Sellwood J. A., Debattista V. P., 2009, MNRAS, 398, 1279
Sellwood J., Kahn F., 1991, MNRAS, 250, 278
Stadel J., 2001, PhD thesis, Univ. Washington
Stinson G., Seth A., Katz N., Wadsley J., Governato F., Quinn T., 2006, MNRAS, 373, 1074
Tinsley B., 1975, ApJ, 197, 159
Torrence C., Compo G. P., 1998, Bull. Am. Meteorol. Soc., 79, 61
Valenzuela O., Klypin A., 2003, MNRAS, 345, 406
Vlajić M., Bland-Hawthorn J., Freeman K. C., 2011, ApJ, 732, 7
Wadsley J., Stadel J., Quinn T., 2004, New Astron., 9, 137
Weinberg M., Katz N., 2007, MNRAS, 375, 425
Wielen R., 1977, A&A, 60, 263
Wielen R., Fuchs B., 1985, in van Woerden H., Allen R., Burton W., eds, Proc. IAU Symp. 106, The Milky Way Galaxy. Reidel, Dordrecht, p. 481
Wielen R., Fuchs B., Dettbarn C., 1996, A&A, 314, 438
Williams B., Dalcanton J., Dolphin A., Holtzman J., Sarajedini A., 2009, ApJ, 695, L15
Wilson M. L. et al., 2011, MNRAS, 413, 2235
Yanny B. et al., 2009, AJ, 137, 4377
Yoachim P., Roškar R., Debattista V., 2010, ApJ, 716, L4
Yoachim P., Roškar R., Debattista V. P., 2012, ApJ, 752, 97

This paper has been typeset from a TEX/LATEX file prepared by the author.